

Contents lists available at ScienceDirect

Petroleum Science

journal homepage: www.keaipublishing.com/en/journals/petroleum-science



Original Paper

Complementary testing and machine learning techniques for the characterization and prediction of middle Permian tight gas sandstone reservoir quality in the northeastern Ordos Basin, China



Zi-Yi Wang ^a, Shuang-Fang Lu ^{b, c, *}, Neng-Wu Zhou ^{b, c}, Yan-Cheng Liu ^d, Li-Ming Lin ^d, Ya-Xin Shang ^a, Jun Wang ^a, Guang-Shun Xiao ^a

- ^a State Key Laboratory of Deep Oil and Gas, China University of Petroleum (East China), Qingdao, 266580, China
- ^b Sanya Offshore Oil & Gas Research Institute, Northeast Petroleum University, Sanya, 572025, Hainan, China
- ^c Key Laboratory of Continental Shale Hydrocarbon Accumulation and Efficient Development, Ministry of Education, Northeast Petroleum University, Daging, 163318, Heilongjiang, China
- ^d China United Coalbed Methane Corporation Ltd., Beijing, 100083, China

ARTICLE INFO

Article history: Received 10 August 2022 Received in revised form 10 May 2024 Accepted 25 August 2024 Available online 29 August 2024

Edited by Teng Zhu and Jie Hao

Keywords:
Diagenetic facies
Reservoir quality
Wireline log prediction
Machine learning techniques
Tight gas sandstones

ABSTRACT

In this study, an integrated approach for diagenetic facies classification, reservoir quality analysis and quantitative wireline log prediction of tight gas sandstones (TGSs) is introduced utilizing a combination of fit-for-purpose complementary testing and machine learning techniques. The integrated approach is specialized for the middle Permian Shihezi Formation TGSs in the northeastern Ordos Basin, where operators often face significant drilling uncertainty and increased exploration risks due to low porosities and micro-Darcy range permeabilities. In this study, detrital compositions and diagenetic minerals and their pore type assemblages were analyzed using optical light microscopy, cathodoluminescence, standard scanning electron microscopy, and X-ray diffraction. Different types of diagenetic facies were delineated on this basis to capture the characteristic rock properties of the TGSs in the target formation. A combination of He porosity and permeability measurements, mercury intrusion capillary pressure and nuclear magnetic resonance data was used to analyze the mechanism of heterogeneous TGS reservoirs. We found that the type, size and proportion of pores considerably varied between diagenetic facies due to differences in the initial depositional attributes and subsequent diagenetic alterations; these differences affected the size, distribution and connectivity of the pore network and varied the reservoir quality. Five types of diagenetic facies were classified: (i) grain-coating facies, which have minimal ductile grains, chlorite coatings that inhibit quartz overgrowths, large intergranular pores that dominate the pore network, the best pore structure and the greatest reservoir quality; (ii) quartz-cemented facies, which exhibit strong quartz overgrowths, intergranular porosity and a pore size decrease, resulting in the deterioration of the pore structure and reservoir quality; (iii) mixed-cemented facies, in which the cementation of various authigenic minerals increases the micropores, resulting in a poor pore structure and reservoir quality; (iv) carbonate-cemented facies and (v) tightly compacted facies, in which the intergranular pores are filled with carbonate cement and ductile grains; thus, the pore network mainly consists of micropores with small pore throat sizes, and the pore structure and reservoir quality are the worst. The grain-coating facies with the best reservoir properties are more likely to have high gas productivity and are the primary targets for exploration and development. The diagenetic facies were then translated into wireline log expressions (conventional and NMR logging). Finally, a wireline log quantitative prediction model of TGSs using convolutional neural network machine learning algorithms was established to successfully classify the different diagenetic facies.

© 2024 The Authors. Publishing services by Elsevier B.V. on behalf of KeAi Communications Co. Ltd. This is an open access article under the CC BY license (http://creativecommons.org/licenses/by/4.0/).

1. Introduction

ute, Northeast
Tight gas sandstones (TGSs) are valuable resources worldwide.
TGSs are found in reservoirs with permeabilities in the micro-Darcy

^{*} Corresponding author. Sanya Offshore Oil & Gas Research Institute, Northeast Petroleum University, Sanya, 572025, Hainan, China. E-mail address: lushuangfang@upc.edu.cn (S.-F. Lu).

Z.-Y. Wang, S.-F. Lu, N.-W. Zhou et al. Petroleum Science 21 (2024) 2946–2968

range and low porosities and have large gas reserves and future production potential (Khlaifat et al., 2011; Desbois et al., 2011; Zou et al., 2013). Many TGS-containing basins throughout the world are already in the exploration or production stages (Law and Curtis, 2002; Shanley et al., 2004; Rushing et al., 2008; Ma et al., 2016) and play a significant part in the global energy pyramid. Precise TGS reservoir quality knowledge and forecasting help researchers identify better zones of production (sweet spots) where commercial value can be obtained, thereby reducing exploration risk and making it possible to predict well production and evaluate volumetric reserves (Hood and Yurewicz, 2008; Xiao et al., 2017; Wang et al., 2023a, 2023b).

The Linxing field is a new TGS field located in the northeastern Ordos Basin (Mi and Zhu, 2021; Wang et al., 2023c). The middle Permian Shihezi Formation is one of the most important TGS reservoirs in the Linxing field (Gao et al., 2019; Mi and Zhu, 2021). Before uplift, the maximum paleoburial depth of the Shihezi Formation in the study area reached 2500-2800 m (Shu et al., 2019; Guo et al., 2021). Deep burial resulted in the TGSs of the Shihezi Formation undergoing high degrees of diagenetic alteration and having low porosities and micro-Darcy-range permeabilities (Qi et al., 2020; Shu et al., 2021; Guo et al., 2021, Wang et al., 2023d). Previous studies have analyzed how the depositional environment controls the reservoir quality of TGSs in the Shihezi Formation and have indicated that high-quality reservoirs usually formed in deltaic distributaries (Liu et al., 2018; Liu et al., 2018). Typically, reservoir quality heterogeneity in TGSs is often linked to initial sedimentary characteristics and subsequent diagenetic alterations (Sadhukhan et al., 2007; Rushing et al., 2008; Morad et al., 2010; Nabawy and Géraud, 2015; Lai et al., 2018a; Qiao et al., 2020; Wang et al., 2023b). The original rock characteristics present during deposition were quite different from the current characteristics if the reservoir rock has undergone extensive diagenesis (Rushing et al., 2008; Morad et al., 2010; Li et al., 2021). Therefore, despite the progress made in research on TGS reservoirs in the Shihezi Formation, effective TGS exploitation still requires a comprehensive reservoir characterization program because it is likely useless and inefficient if the depositional environment and the accompanying depositional rock types (in isolation) are used as guides.

The initial pore space is determined by the sedimentary composition and textural parameters of the sandstone (Morad et al., 2010; Ajdukiewicz and Lander, 2010). Pore structures are significantly reshaped by different types and degrees of diagenesis (Sadhukhan et al., 2007; Nabawy and Géraud, 2015; Lai et al., 2018a; Qiao et al., 2020). One method for analyzing reservoir heterogeneity is rock typing, which involves examining, describing, and interpreting the sedimentary and petrophysical features of various kinds of rocks (Rushing et al., 2008; Ma et al., 2016; Lai et al., 2018a). The main rock typing methods include deposit facies classification, electrofacies classification, hydraulic flow unit classification, and diagenetic facies classification (Rahimpour-Bonab et al., 2012; Kadkhodaie-Ilkhchi and Rezaee, 2013; Lai et al., 2018a; Mehrabi et al., 2019a, 2019b; Bahrehvar et al., 2021; Mehrabi and Bagherpour, 2022; Foroshani et al., 2023). The diagenetic facies method is a rock typing method that was developed specifically for tight sandstones that incorporates the outcomes of depositional and diagenetic processes and provides thorough descriptions of the extent of diagenetic alterations and types of diagenetic minerals (Zou et al., 2008; Lai et al., 2018b). Previous studies have demonstrated that diagenetic facies can be used to analyze the reservoir quality heterogeneities of TGSs and to make reasonable predictions of the distribution of reservoirs in the subsurface (Liu et al., 2015; Lai et al., 2018b, 2019, 2020; Cao et al., 2021).

Since wireline logs are less costly to acquire than cores, advanced knowledge of the reservoir quality of TGSs by wireline

logs is critical for the commercial production of low-permeability and heterogeneous TGS reservoirs. It is challenging to properly distinguish between TGS reservoirs using wireline cross-plots or cutoff approaches because of the complex and heterogeneous petrophysical properties of TGS reservoirs (Ma et al., 2016). Many machine learning-based techniques that to improve the efficiency and accuracy of petrophysical classification have recently been developed (AversAnA et al., 2019; Antariksa et al., 2022; Kim, 2022). The major goal of these techniques is to identify mathematical or geographical correlations between petrophysical implications and wireline data by allowing computers to quickly execute iterative computations with extremely complicated equations (Misra et al., 2019; Kim, 2022). TGS fields require the analysis of a large amount of well data due to complex geological conditions, and a data-driven machine learning-based approach can be used to establish or update field development plans in a timely manner. Another advantage of introducing machine learning techniques is that they can be used to prevent, to some extent, the uncertainty associated with bias or accidental errors in manual logging interpretation (Ma and Gomez, 2015; Al Khalifah et al., 2020).

In this study, optical light microscopy, cathodoluminescence (CL), standard scanning electron microscopy (SEM), whole-rock X-ray diffraction (XRD), porosity and permeability measurements, mercury intrusion capillary pressure (MICP) measurements, nuclear magnetic resonance (NMR) measurements, and rock mechanics tests were used to classify the diagenetic facies of the Shihezi Formation TGSs, and detailed characterization of their reservoir quality was then conducted. Subsequently, the response characteristics of the diagenetic facies and wireline logs (conventional logging and NMR logging) were summarized, and a quantitative wireline log prediction model for diagenetic facies based on a convolutional neural network (CNN) machine learning algorithm was constructed. The objectives of this study are to provide a systematic scheme to evaluate and predict the reservoir quality of TGSs in the study area and similar regions.

2. Geological background

The Ordos Basin is located in the western part of the North China Block and is a typical polycyclic cratonic basin (Fig. 1) (Yang et al., 2005; Liu et al., 2016; Sun and Dong, 2019). The Ordos Basin is divided into six secondary tectonic units: the Yimeng Uplift, the Weibei Uplift, the Jinxi Fault-Fold Belt, the Yishan Slope, the Tianhuan Depression, and the Western Thrust Belt (Fig. 1) (Xiao et al., 2005; Hanson et al., 2007). The Linxing area is located in the Jinxi Fault-Fold Belt on the northeastern margin of the Ordos Basin (Fig. 1).

During the deposition of the middle Permian Shihezi Formation, braided river delta environments were present in the study area (Mi and Zhu, 2021). The middle Permian strata consist of gray-black to white, relatively massive, fine-to coarse-grained sandstone, minor thin siltstone, and mudstone with thicknesses of approximately 400 m (Fig. 1). The primary TGS reservoir in the study region is composed of distributary and natural levee sandstones (Fig. 2).

3. Data and methods

3.1. Imaging methods

In this study, optical light microscopy, CL, and SEM were used to image the samples. Entire thin sections were examined in two dimensions under plane-polarized light to determine the mineralogy, texture, and pore system of the samples. CL clearly revealed various diagenetic minerals, such as quartz cement, calcite cement, and kaolinite. High-resolution images of diagenetic minerals with

Z.-Y. Wang, S.-F. Lu, N.-W. Zhou et al. Petroleum Science 21 (2024) 2946–2968

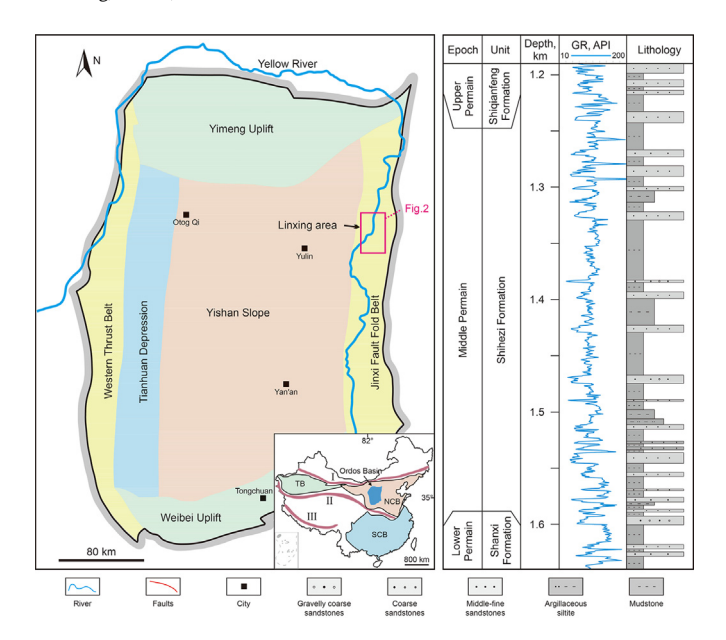


Fig. 1. Tectonic units of the Ordos Basin and the stratigraphy of the middle Permian Shihezi Formation in the Linxing field. Sun and Dong's (2019) map of China has been modified. I: Central Asian Orogenic Belt; II: Central China Orogenic Belt; III: Himalayan Orogenic Belt. TB: Tarim Block; NCB: North China Block; SCB: South China Block.

different structural habits were obtained via SEM, and the pore system associated with authigenic clay minerals was detected. All thin sections were examined using a Zeiss Axioscope and a Leica DM4P microscope. For CL analysis, an Axiolmager A2m cathodoluminescence microscope was used. A Zeiss Crossbeam 550 focused ion beam scanning electron microscope with a test environment of 10% humidity and 23 °C was used for SEM analysis.

P25 and P75 are the particle sizes (mm) that correspond to 25% and 75% on the grain size cumulative frequency curve, respectively (Eq. (1)). The Trask sorting coefficient (S_0) was used to compute the original porosity (OP) at the time of deposition (Eq. (2)) (Beard and Weyl, 1973). The intergranular volume (IGV) is the total volume of the main porosity, pore-filling cement (CEM), and matrix material (Ehrenberg, 1989). Following known norms (Eqs. (3) and (4)), point count data were utilized to compute the IGV, compaction porosity loss (COPL), and cemented porosity loss (CEPL).

$$S_0 = P_{25}/P_{75} \tag{1}$$

$$OP = 20.91 + 22.9/S_0 \tag{2}$$

$$COPL = OP - \frac{(100 \times IGV) - (OP \times IGV)}{100 - IGV}$$
(3)

$$CEPL = \frac{(OP - COPL) \times CEM}{IGV}$$
 (4)

3.2. Whole-rock XRD analysis

Whole-rock XRD analysis was successful in identifying the contents of quartz, feldspar, carbonate, and clay minerals. All samples were examined using a D/max-2600 X-ray diffraction instrument at 40% humidity and $25\,^{\circ}$ C.

3.3. Porosimetry and permeability

Gas expansion (He porosimetry) was employed to measure the rock porosity and permeability. Porosimetry and permeability were measured using a U1tra-Porotm 300 porosimeter and FCG-059VINCI permeability tester, respectively. The ambient temperature during the test was 25 °C, and the atmospheric pressures were 102.4—103.2 kPa.

3.4. MICP experiments

MICP is an approach that is typically used for assessing pore properties, notably the distribution of pore throat sizes in porous media. The MICP data are also indicative of various pore space features. The MICP instrument used to analyze all the samples in this study was an Autopore IV 9500 mercury porosimeter. Samples with a diameter of 2.5 cm under vacuum conditions were tested on an Autopore IV 9500 mercury porosimeter at an ambient temperature of 15 $^{\circ}\text{C}$.

3.5. NMR experiments

NMR is a sophisticated, nondestructive, and quantitative tool for

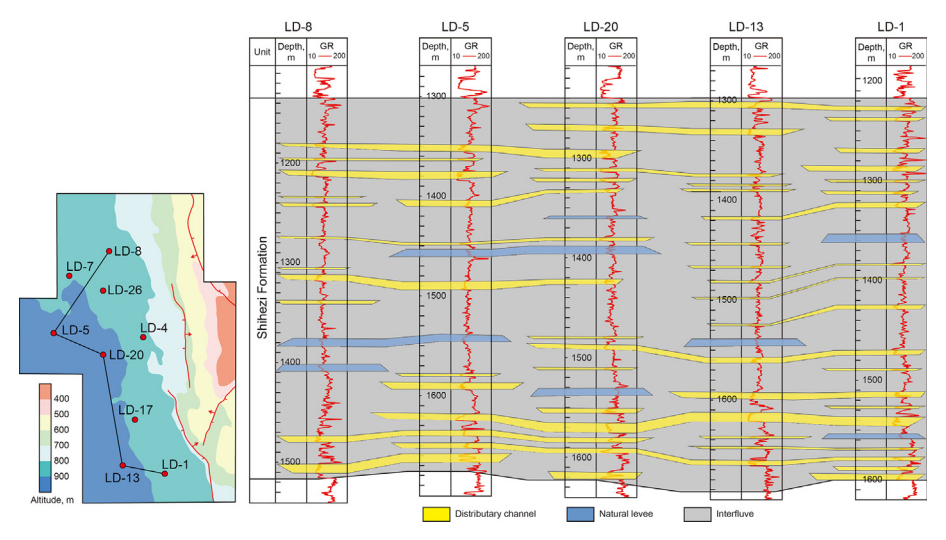


Fig. 2. The locations of the investigated wells as well as their sedimentological and gamma-ray (GR) logs.

examining the pore structure (Zhang et al., 2018; Li et al., 2019). The T_2 relaxation time (initial and cumulative) distributions of the core plug samples were analyzed after 100% brine saturated centrifugation. The amplitude of the T_2 spectrum (Y-axis) is directly correlated with the sample porosity, and the T_2 time (X-axis) is proportional to the pore size. The T_2 spectrum was transformed into the pore throat size using MICP data, following a methodology meticulously delineated in prior studies by Xiao et al. (2016) and Huang et al. (2018). To determine the bound water status, core samples with a diameter of 2.5 cm were centrifuged after being completely saturated with brine. At 25 °C, a MesoMR23-040H-1 low-field nuclear magnetic resonance analyzer was used to determine the NMR T_2 relaxation time for brine-saturated, centrifuged core plugs.

3.6. Wireline log data

Conventional wireline logs; natural gamma ray (GR) logs; three porosity logs, namely, acoustic transit time (AC), bulk density (DEN) and compensated neutron log (CNL) logs; and resistivity logs (RT), which are susceptible to variations in the diagenetic type and intensity, were used (Liu et al., 2015; Cui et al., 2017; Lai et al., 2018b, 2019, 2020). The unimodal and bimodal T₂ distributions from NMR logging revealed the pore structure, indicating the pore connectivity and formation heterogeneity (Solanet et al., 1998; Jacobsen et al., 2006; Freedman, 2006). The correlation of wireline log data with core analytical data allows for diagenetic facies prediction. Combining traditional wireline logging with NMR logging enables the various diagenetic facies to be precisely identified and provides reservoir quality information. All logging data were provided by the China United Coalbed Methane Company.

3.7. Background information of the convolutional neural network model

Convolutional neural networks (CNNs) were used to solve machine learning algorithms for diagenetic facies classification. CNNs have the advantages of local connectivity, weight sharing, downsampling and dimensionality reduction. Unlike artificial neural networks (ANNs), which compute the entire input data simultaneously through a network of fully connected neurons, CNNs are designed to process specific combinations between data elements. In oil and gas geophysics, CNNs have been effectively used for seismic data interpretation tasks, such as fault detection, facies classification, and amplitude versus offset (AVO) analysis. These tasks involve analyzing 2D or 3D seismic data arrays, where CNNs have demonstrated significant effectiveness. The 1-D CNN uses one-dimensional kernels to efficiently process linear data and is ideal for extracting features from segments of the dataset, irrespective of their position. Recent research has shown that CNN algorithms may also be used to forecast the petrophysical properties of subsurface rocks by fusing 1D wireline logging data with CNN algorithms (Wei et al., 2019; Imamverdiyev and Sukhostat, 2019; Kim et al., 2022). CNNs are adept at detecting petrophysical features from wireline logs and identifying various geological indicators, such as the hydrocarbon presence and secondary porosity.

To develop a diagenetic facies machine learning classification system, we employed a comprehensive and systematic data-driven modeling approach involving the following key steps (Fig. 3a).

a Gathering ample pertinent data is essential for achieving credible outcomes when deploying machine learning algorithms for any learning task. In this study, core analysis data from nine wells served as the basis for classifying diagenetic facies.

- b For the aforementioned nine wells used for the core analysis, we procured well logs and constructed training and testing sets to assess the model's performance.
- c Data preprocessing. The well log data collected in the second step typically require preprocessing before they can be effectively utilized by machine learning algorithms. This process included addressing and removing missing values.
- d A deep convolutional neural network was developed to classify well diagenetic facies, and the model was fully optimized using well log data and core data to ensure the most efficient and accurate solution.
- e The performance of the developed classifier was evaluated via its application to an unknown log dataset.

A schematic representation of the CNN algorithm is shown in Fig. 3b. The study's input comprises the 1D wireline logs; each data point represents measurements (GR, AC, DEN, CNL, and RT) at specific depths, which fundamentally differs from the 2D image data. In this context, each depth point forms a 1D array with 5 channels. CNNs apply convolutional filters along the depth point, thereby analyzing patterns in log measurements to identify geological features.

The input layer intakes well logging data, and proceeds to the convolution stage, which comprises convolutional and pooling layers. A defined number of filter windows (kernels) are utilized for extracting features. During this stage, the input data undergo a convolution operation by employing a specified number of filters, which is mathematically represented as follows:

$$s_1(t) = (x * f_1)(t) = \sum_{k=1}^{K} x_{t+k-1} \cdot f_{1k}$$
 (5)

In this equation, "x" represents the input one-dimensional data sequence, which are the wireline log data (GR, AC, DEN, CNL, and RT) at depth point "t"; " f_1 " represents the filters utilized in the first convolutional layer; "K" signifies the filter size; and " $s_1(t)$ " is the result from the convolutional operation.

The pooling layer plays a pivotal role in reducing computational complexity and isolating secondary features. In our study, we opted for maximum pooling, as the alternative, i.e., average pooling, tends to minimize disparities within the pooling area, potentially leading to the loss of valuable information. Although maximum pooling is vulnerable to noise, including extreme values due to measurement errors, the input data for this study underwent preprocessing to remove this noise. Furthermore, a consistent caliper log enhances the reliability of the data.

Following the convolution process, a fully connected stage was implemented. This stage employed a general artificial neural network comprising several hidden and output layers. To transition from the convolution to the fully connected stage, the output of the convolution stage was transformed into a one-dimensional array. The optimal numbers of neurons and hidden layers were determined through a random search function to identify the best parameters.

To address the nonlinear characteristics of the dataset, the ReLu function (Eq. (6)) was employed. This function converts negative values in the feature map to zero, preserving positive outputs. It enables the machine learning model to perform rapid calculations and mitigates issues related to gradient disappearance during model training.

$$h_1(t) = \max(0, s_1(t))$$
 (6)

The precision of our model's predictions was quantified using the cross-entropy loss function, which is encapsulated by the

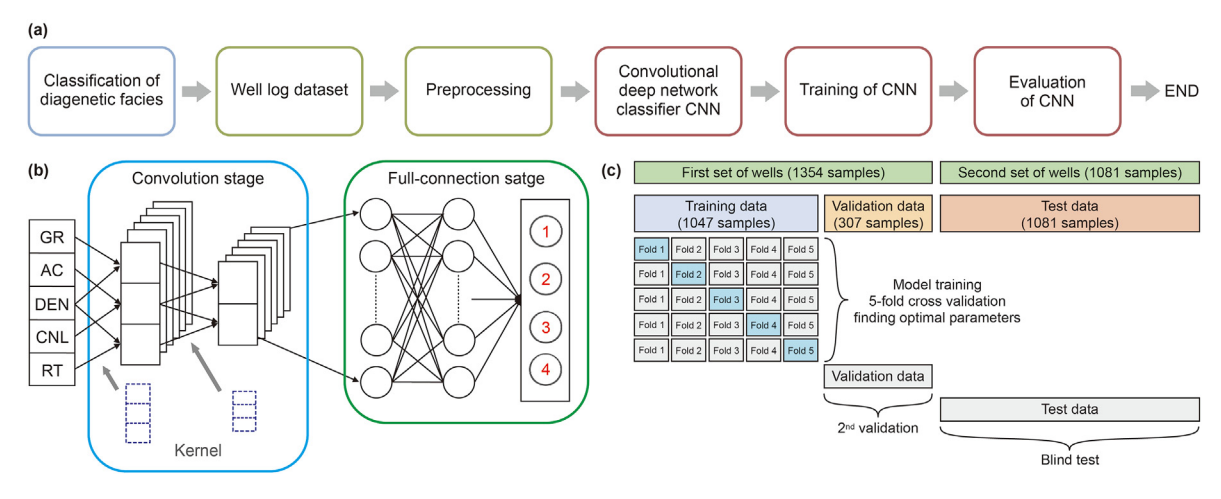


Fig. 3. Schematic structure of the (a) diagenetic facies classification process using CNN algorithms, (b) CNN model (Modified from Kim, 2022), and (c) validation and test process.

following formula:

$$L = -\sum_{c=1}^{C} y_{0,c} \log \left(p_{0,c} \right)$$
 (7)

C is the total number of categories, and $y_{0,c}$ is a binary indicator that is 1 when sample o belongs to category c and 0 otherwise. $p_{0,c}$ is the predicted probability that sample o belongs to category c.

3.8. Establishing data for the machine learning model

The first set of input wells (LD-4, LD-5, and LD-17) was utilized for training and validating the CNN algorithm, while the second set (LD-1, LD-7, and LD-13) was reserved for a blind test (Fig. 2). The first set comprised 1354 data samples, which were randomly mixed for training purposes (Fig. 3c). The CNN model was initially developed using these training data. To ensure its reliability, two validation methods were employed. The first method was 5-fold cross-validation, where the training data were divided into five subsets (Fig. 3c). Four of these subsets were used for training the model, and the fifth subset was used for validation. This approach was used to test the model's consistency across the different training datasets and enabled the full utilization of training data without losing any samples. The second method involved using separate validation data that were not part of the training set; this provided an additional evaluation of the model's performance with unfamiliar data. After satisfactory results were achieved from both validation methods, the model was applied to the second set of wells, which included 1081 samples (Fig. 3c), Notably, 307 samples from the first set were not used in training the model, and the entire dataset of the second set (1081 samples) was kept separate for testing. This approach was designed to assess the model's applicability to both partially and fully uncored intervals in cored wells. Although core data from both sets of wells were obtained for direct diagenetic facies interpretation, this study was structured to rely solely on wireline log data, without core data, for certain drilling intervals. The CNN model's predictions of diagenetic facies were then compared with the actual interpretations derived from the core data.

The confusion matrix, which provides detailed statistics on correctly and incorrectly classified formations, was employed to assess the CNN model's classification performance. The total correct percentage was used as a validation metric (Eq. (8)):

Total correct percentage = Successful cases in the classification/

total cases (Eq. (8)).

3.9. Hyperparameter tuning

To identify the optimal hyperparameters, a random search function was applied to the CNN model, and five key hyperparameters, as detailed in Table S1, were tested. Hyperparameter ranges were established through manual trials, followed by a random search to identify the optimal settings. Default values were used for additional hyperparameters (Table S2). The iteration's best parameter set was then utilized in the second phase of validation and testing.

4. Results

4.1. Texture and composition

The Shihezi Formation TGSs include subarkose, sublitharenite, arkose, lithic arkose and feldspathic litharenite, according to Folk's (1980) classification (Fig. 4).

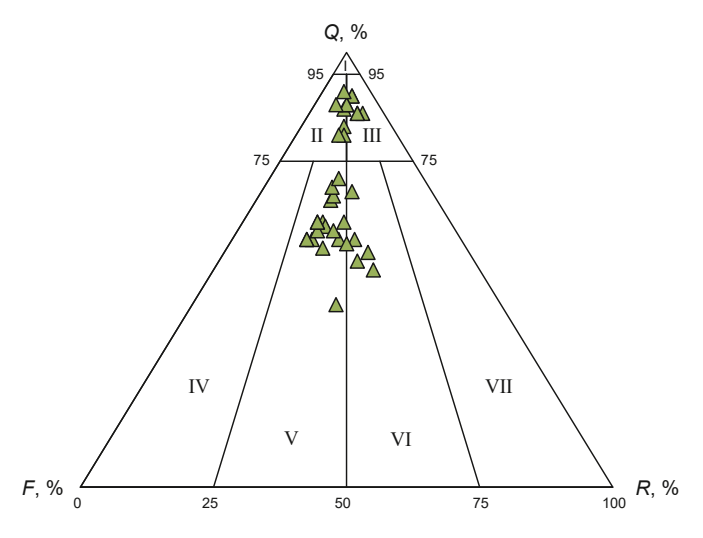


Fig. 4. Ternary diagram classification of the sandstones in the Shihezi Formation using Folk's (1980) classification. I: quartz arenite; II: subarkose; III: sublitharenite; IV: arkose; V: lithic arkose; VI: feldspathic litharenite; VII: litharenite. Q: quartz, metaquartzite; f: feldspar, granite and gneiss fragments; R: all other rock fragments (include chert).

The TGSs of the Shihezi Formation are fine-grained to gravelly sandstones (Fig. 5a-f). Most of the detrital grains are subangular and subrounded (Fig. 5a-f). The monocrystalline quartz grain contents range from 28% to 84% (mean of 50%) (Table 1). The polycrystalline quartz grain contents range from 4% to 43% (mean of 22%) (Table 1). The most prevalent feldspar component is K-feldspar, the contents of which range from 3% to 23% (mean of 9.4%) (Table 1). The plagioclase contents vary from 1% to 14% (mean of 7%) (Table 1). The lithic fragments include igneous rock fragments (with contents of 2%-17% and a mean of 7%), metamorphic rock fragments (with contents of 0%-10% and a mean of 3%) and minor sedimentary rock fragments (mean of 0.3%) (Table 1). Biotite is prevalent in fine-grained sandstones, accounting for 0%-3% (mean of 0.6%) of the total rock volume (Table 1 and Fig. 5a). The TGSs of the Shihezi Formation also contain different proportions of detrital clay matrix (Fig. 5b).

4.2. Diagenetic features

4.2.1. Compaction

Compaction by lithostatic pressure causes a reorganization of the rock composition and changes in its contact geometry (Rezaee and Lemon, 1996). Rigid grains, such as quartz, in the TGSs of the Shihezi Formation are typically arranged along line contacts (Fig. 5a and b). Ductile grains (clay-rich rock fragments, detrital clay matrix, and mica) are often in concave-convex contact with rigid grains (Fig. 5a and b). Optical light microscopy revealed that ductile particles, such as biotites, are severely deformed under mechanical action and compressed between harder quartz and feldspar grains to form a pseudomatrix (Fig. 5a and b).

4.2.2. Authigenic minerals

The main authigenic mineral cements found in the TGSs of the Shihezi Formation include carbonate, quartz, and clay mineral cements.

Almost all the observed carbonate cements are calcite. The calcite is dull red to orange—yellow under CL (Fig. 5c). Calcite shows two forms of development: filling large primary intergranular pores (Fig. 5c and d) or filling small pores between closely packed grains (Fig. 5e). Calcite fills in the primary intergranular pores, resulting in framework grain particles displaying a floating texture; this texture occludes pores and replaces the framework grains, which are stained pink (Fig. 5d). Calcite filling small pores within the grains occurs as small irregular patches, even locally replacing clastic grains, and the calcite is purple when stained with alizarin, indicating that the calcite contains iron (Fig. 5e). Based on petrographic evidence, the formation of ferroan calcite postdates quartz overgrowths (Fig. 5e).

Quartz cements occur as quartz overgrowths (Fig. 5f and g) and microquartz crystals (Fig. 5h and i). Quartz overgrowths are more common in coarse sandstones that do not contain chlorite coatings (Fig. 5l and m). Microquartz crystals intercalated with clay minerals developed within pore spaces (Fig. 5h), and microquartz crystals found as single hexagonal bipyramidal crystals are clearly visible under SEM (Fig. 5i). According to petrographic observations, the formation of quartz cements postdates the chlorite coatings (Fig. 5l and m).

The clay mineral cements in the TGSs of the Shihezi Formation include illite, chlorite, and kaolinite. The CL color of kaolinite is blue (Fig. 5j), and kaolinite fills pores as euhedral hexagonal crystal aggregates (called 'books') (Fig. 5k and o). Illite occurs as ribbonlike filaments and as bridging "hairs" in the pores (Fig. 5h and i). Chlorite cement usually takes the form of radial detrital grain coatings composed of euhedral, interconnecting plates (Fig. 5i and m). Quartz overgrowths in sandstones, where chlorite coatings are

present, are usually not developed (Fig. 5i).

4.2.3. Dissolution

Dissolution commonly occurs in the TGSs of the Shihezi Formation. Dissolution occurs mainly in feldspars (Fig. 5n and 0), and dissolution of diagenetic minerals is negligible. The skeletal feldspar grains observed by thin section and SEM analyses are important evidence of feldspar dissolution (Fig. 5n and 0). Dissolution is relatively rare in sandstones with high clastic mudstone contents (Fig. 5a) and widespread calcite cementation (Fig. 5d).

4.3. Pore systems

The TGSs of the Shihezi Formation contain intergranular pores (primary intergranular pores and residual intergranular pores) and intragranular pores (intragranular dissolution pores and clay mineral intercrystalline micropores) (Fig. 6). Primary pores refer to the pores existing in sand at the time of its deposition (Worden and Burley, 2003). Chlorite coatings usually occur at the interfaces between clastic grains and primary intergranular pore spaces (Fig. 6a). Typically, in primary intergranular pores, no diagenetic cement, other than chlorite coatings, is present, and the pore sizes are large (Fig. 6a). The precipitation of pore-filling cements (mainly authigenic quartz) within primary intergranular pores changes the pore shape, size, and overall volume, and they are transformed into residual intergranular pores (Fig. 6b and c). The pore sizes of the residual intergranular pores are significantly smaller than those of the primary intergranular pores (Fig. 6b and c). The dissolution of chemically unstable feldspars results in the formation of dissolution pores (Fig. 6b and d). Given that completely dissolved clastic feldspars are uncommon, large intergranular dissolution pores are rare, and most are intragranular dissolution pores (Fig. 6b and d). Intercrystalline micropores are primarily visible in clay minerals, such as kaolinite and illite, according to SEM images. By subtracting the macroporosity determined by point counting from the total porosity determined from core analysis, the microporosity was computed (Worden et al., 2000).

5. Discussion

5.1. Diagenetic facies classification

Diagenetic facies are identified and classified through petrographic observations and SEM analysis, employing a process-based classification as defined by Lai et al. (2018b). This classification relies on the compositional and textural attributes, diagenetic minerals, and pore systems of reservoir rocks. Typically, specific diagenetic facies exhibit consistent compositional and textural attributes, matrix and cement compositions, and pore systems (Cui et al., 2017; Lai et al., 2019, 2020; Cao et al., 2021).

In this study, based on the detrital composition, diagenetic minerals and pore type assemblages, the TGSs of the Shihezi Formation are divided into five diagenetic facies: grain-coating facies, quartz-cemented facies, mixed-cemented facies, carbonate-cemented facies, and tightly compacted facies (Table 2). The composition and texture of sandstone, including the grain size and ductile grain content, serve as indicators of the sedimentary environment. Authigenic minerals and pore systems, on the other hand, reflect diagenetic processes (Table 2). This approach is valuable for describing the diagenetic history, assessing the reservoir quality, and predicting sweet spots.

5.1.1. Grain-coating facies

The coarsest grain sizes (average of 394 µm) and least ductile grain contents (average of 2.67%) are present in the grain-coating

Z.-Y. Wang, S.-F. Lu, N.-W. Zhou et al. Petroleum Science 21 (2024) 2946–2968

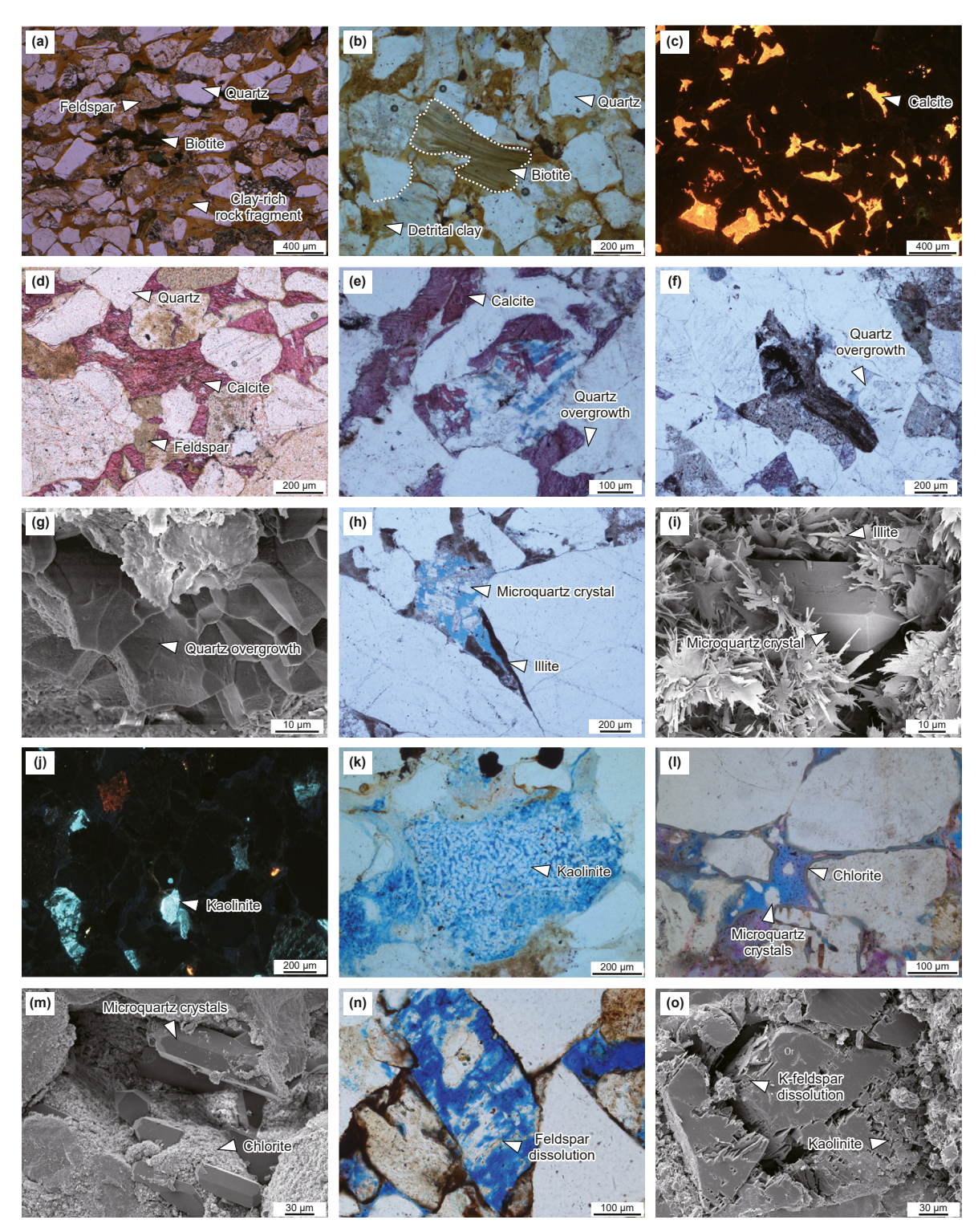


Fig. 5. Photomicrographs of the TGSs in the Shihezi Formation. (a) Detrital clays and biotite flakes showing ductile compaction, Well LD-4, 1536.4 m, depth of 1875.89 m, plane-polarized light (PPL); (b) ductile grains deformed along adjacent rigid grains, Well LD-4, 1589.91 m, PPL; (c) calcite cement occluding intergranular pore space, Well LD-1, 1599.61 m, cathodoluminescence (CL); (d) calcite cement occluding intergranular pore space, forming a "floating grain" texture, Well LD-17, 1382.83 m, PPL; (e) patchy calcite and detrital grain replacement, Well LD-20, 1574.76 m, PPL; (f) quartz overgrowths, Well LD-8, 1516.63 m, PPL; (g) quartz overgrowths, Well LD-20, 1382.36 m, PPL, standard scanning electron microscopy (SEM); (h) microquartz crystals filling pore space, Well LD-20, 1200.55 m, PPL; (i) postquartz overgrowth pore bridging 'hairy' illite, Well LD-20, 1200.55 m, SEM; (j) blue CL color of kaolinite, Well LD-8, 1211.54 m, CL; (k) kaolinite filling pore space, Well LD-3, 1744.52 m, CL; (l) chlorite coatings bordering intergranular pores between detrital granules at their interfaces, Well LD-17, 1388.74 m, PPL; (m) detailed image of enclosed authigenic chlorite, Well LD-8, 1211.54 m, SEM; (n) dissolved feldspar, Well LD-5, 1242.00 m, PPL; (o) partially dissolved feldspar, Well LD-8, 1515.41 m, SEM.

Table 1Petrographic optical point count data of the TGSs in the Shihezi Formation.

Well	Depth, m	Quartz		Feldspar		Igneous rock	Metamorphic rock	Sedimentary rock	Detrital
		Monocrystalline quartz, %	Polycrystalline quartz, %	Plagioclase, %	K-feldspar, %	fragment, %	fragment, %	fragment, %	biotite, %
LD-4	1290.4	30	38	10	12	8	2	0	0
LD-4	1297.5	42	26	8	10	10	2	0	0
LD-5	1558.0	34	26	8	16	12	2	1	1
LD-5	1559.7	33	25	10	10	17	3	1	1
LD-5	1588.6	46	20	13	7	10	1	0	3
LD-5	1589.0	38	29	13	6	8	1	0	2
LD-5	1589.4	28	33	11	13	9	2	2	2
LD-5	1590.5	38	19	14	14	10	1	0	1
LD-5	1653.2	28	31	10	12	16	1	1	1
LD-7	1676.7	30	43	4	15	7	0	0	1
LD-8	1211.5	78	10	2	4	5	0	0	0
LD-8	1212.3	80	8	3	5	4	0	0	0
LD-8	1213.3	81	10	1	4	3	1	0	0
LD-8	1511.7	81	5	2	3	3	4	1	0
LD-8	1512.0	84	6	1	3	2	4	0	0
LD-8	1512.6	83	4	3	4	3	3	0	0
LD-8	1514.3	70	16	1	4	2	4	0	1
LD-8	1514.8	66	22	2	4	2	3	0	1
LD-8	1515.4	63	6	6	4	2	3	1	0
LD-8	1516.2	61	22	3	6	3	2	0	1
LD-13	1737.5	42	29	6	11	9	2	0	0
LD-17	1233.0	33	27	10	14	6	10	0	0
LD-17	1233.4	34	31	9	12	6	8	0	0
LD-17	1235.6	36	26	8	17	3	9	0	1
LD-17	1236.4	34	30	13	15	7	0	0	1
LD-17	1382.8	46	26	4	10	10	1	1	0
LD-20	1200.6	51	25	2	5	15	2	0	0
LD-26	1359.7	36	21	13	23	7	0	0	0

facies (Table 3 and Fig. 8a and b). The grain-coating facies is typically characterized by chlorite coatings arranged at the interfaces between clastic grains and intergranular pore spaces (Fig. 7a, b). Minor calcite and quartz overgrowths are present (Table 3 and Fig. 8c and d). The grain-coating facies has a low authigenic clay mineral content (average of 2.8%) (Table 3 and Fig. 8e). The grain-coating facies has a significant number of large primary

intergranular pores (average of 8.0%) (Table 3 and Fig. 7a and b and Fig. 8f).

The COPL values of the grain-coating facies range from 14.4 to 20.8%, with an average of 18.4% (Table 3 and Fig. 9). The CEPL values range from 1.6 to 3.4%, with an average of 2.3% (Table 3 and Fig. 9). These values indicate that the original sedimentary porosity of the grain-coating facies decreased mainly due to compaction. The

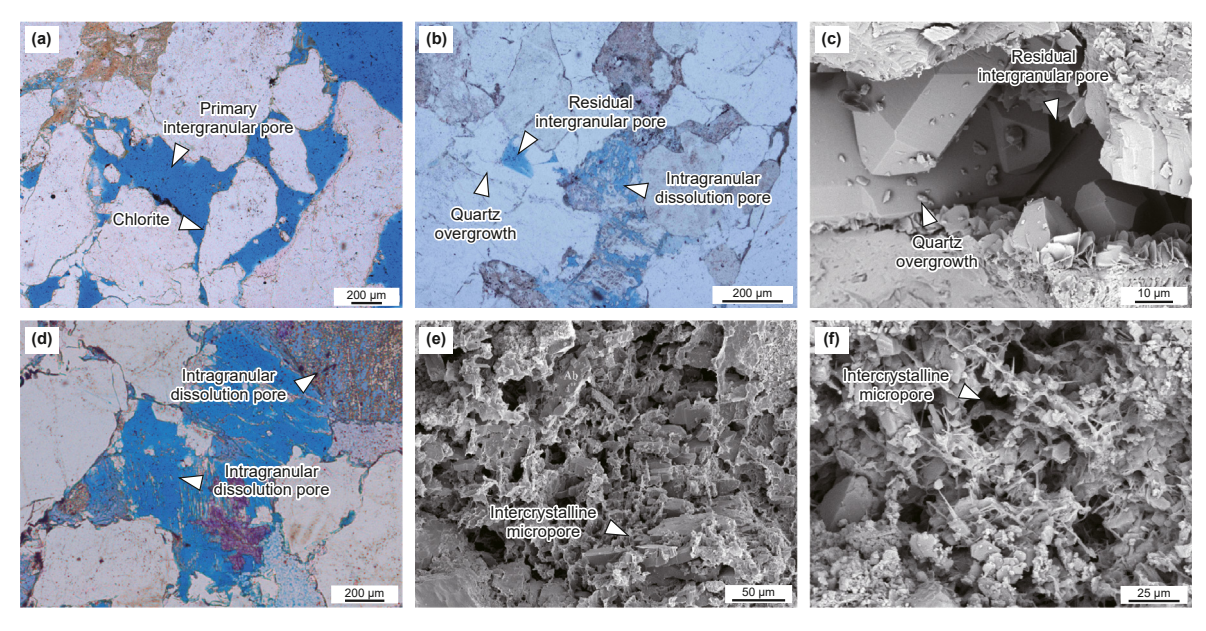


Fig. 6. Optical and SEM images displaying the pore types of TGSs in the Shihezi Formation. (a) Primary intergranular pores, Well LD-17, 1233.36 m, PPL; (b) residual intergranular pores, Well LD-20, 1382.36 m, PPL; (c) residual intergranular pores, Well LD-20, 1382.36 m, SEM; (d) intragranular dissolution pores, Well LD-13, 1738.61 m, PPL; (e) intragranular dissolution pores, Well LD-8, 1212.25 m, SEM; (f) illite containing micropores, Well LD-18, 1131.24 m, SEM.

Table 2Detrital composition, diagenetic minerals and pore type assemblages of various diagenetic facies.

Diagenetic facies	Texture and composition	Diagenetic minerals (features)	Pore type assemblages
Grain-coating facies	Medium- to coarse-grained; low ductile grain content	Moderate mechanical compaction; thin-layer diagenetic chlorite coatings on grain surfaces; rare quartz overgrowths	Primary intergranular pores dominate the pore system, and the system contains a proportion of intragranular dissolution pores and micropores
Quartz-cemented facies	Medium to coarse grained; quartz- grain rich; low ductile grain content	Moderate mechanical compaction; strong quartz overgrowths; pore fillings of authigenic kaolinite/illite	Small numbers of residual intergranular pores and intragranular dissolution pores and micropores
Mixed-cemented facies	Medium-grained; medium ductile grain content	Mechanical compaction; quartz overgrowths; ferroan calcite; pore fillings of authigenic kaolinite/illite	Intragranular dissolution pores, abundant micropores, and almost no intergranular pores
Carbonate-cemented facies	Medium-grained; low to medium ductile grain content; floating texture	Limited mechanical compaction; precipitation of eogenetic carbonate cement	Main porosity contributed by micropores
Tightly compacted facies	Very fine- to medium-grained; high ductile grain content	Mechanical or chemical compaction; absence of diagenetic minerals	Main porosity contributed by micropores

inhibition of quartz overgrowths by chlorite coatings has been widely discussed in previous studies (Nguyen et al., 2013; Stricker and Jones, 2018; Virolle et al., 2022), and petrographic evidence has demonstrated the inhibition of quartz overgrowths by chlorite coatings in the grain-coating facies (Fig. 7a and b). The near absence of calcite cementation, as well as the very low amount of authigenic clay mineral-filled intergranular cement, results in a very low CEPL of the grain-coating facies, thereby preserving many primary intergranular pores.

5.1.2. Quartz-cemented facies

The quartz-cemented facies has the second-largest grain size (average of 359 $\mu m)$ and a ductile grain content (average of 3.6%) (Fig. 8a and b). The quartz-cemented facies shows strong quartz overgrowths (averaging 5.4%) (Table 3 and Fig. 7c and d and Fig. 8c). Calcite cements are almost absent in the quartz-cemented facies, and the authigenic clay mineral content is slightly greater than that in the grain-coating facies (average of 1.0%) (Table 3 and Fig. 8d and e). The strong quartz overgrowths led to a low percentage of primary pores (mainly residual intergranular pores) in the quartz-cemented facies (Fig. 7c, d). Therefore, the average intergranular porosity is only 2.9% (Table 3 and Fig. 8f).

The COPL values of the quartz-cemented facies range from 15.6% to 23.7%, with an average of 19.1% (Table 3 and Fig. 9). The CEPL values range from 5.6 to 9.7%, with an average of 7.8% (Table 3 and Fig. 9). The CEPL of the quartz-cemented facies is greater than that of the grain-coating facies because the quartz-cemented facies lacks the inhibition of quartz overgrowths by chlorite coatings and contains a higher authigenic clay mineral content.

5.1.3. Mixed-cemented facies

The coarsest grain size of the mixed-cemented facies (average of 284 µm) is smaller than that of the two diagenetic facies mentioned above, and the content of ductile grains is greater (average of 7.0%) (Table 3 and Fig. 8a and b). Quartz overgrowths account for 4.3%, and some samples have flakes of iron calcite (4.2% on average) between the grains (Table 3 and Fig. 7e and f and Fig. 8c and d). The mixed-cemented facies have a high authigenic clay mineral content (average of 5.2%) (Table 3 and Fig. 8e). Almost no primary intergranular pores are retained in the mixed-cemented facies (Fig. 7e and f and Fig. 8f). The microporosity percentage is high in some samples, up to an average of 7.2% (Table 3 and Fig. 8h).

The average COPL of the mixed-cemented facies is 17.4% (Table 3 and Fig. 9). The average CEPL is 14.12% (Table 3 and Fig. 9). Compared with the quartz-cemented facies, the mixed-cemented

facies not only has quartz overgrowths but also has a high authigenic clay mineral content, and pore-filling ferroan calcite is present, with a relatively high ductile particle content (biotite and clay-rich rock fragments). This presence causes almost no primary intergranular pores to be preserved in the mixed-cemented facies, and only dissolution pores and micropores are present (Table 3 and Fig. 7e and f).

5.1.4. Carbonate-cemented facies

The carbonate-cemented facies has median sizes with an average of 306 μ m (Fig. 8a and Table 3). Calcite (average of 20.8%) fills in the large intergranular pores (Table 3 and Fig. 7g). No quartz overgrowths are present (Table 3 and Figs. 7g and 8f). No primary intergranular pores are retained in the carbonate-cemented facies, dissolution pores formed by feldspar dissolution are rarely visible (average of 1.25%), and the main porosity is contributed by micropores (average of 3.5%) (Table 3 and Fig. 8g and h).

The carbonate-cemented facies COPL values range from 5.7% to 14.4%, with an average of 10.1% (Table 3 and Fig. 9). The CEPL values range from 18.0% to 26.4%, with an average of 21.0% (Table 3 and Fig. 9). The eogenetic origin of carbonate cements filling large intergranular pores can increase the pressure resistance of sandstones, and therefore, mechanical compaction is limited (Rossi et al., 2001; Morad et al., 2010).

5.1.5. Tightly compacted facies

The tightly compacted facies has the finest grain size (average of 233 $\mu m)$ and the highest ductile grain content (average of 13.2%) (Table 3 and Fig. 8a and b). Quartz overgrowths are absent (Table 3 and Fig. 7h and i and Fig. 8c). The calcite cement content is very low (average of 1.4%) (Table 3, Fig. 8d). As with the carbonate-cemented facies, the tightly compacted facies have a low percentage of intragranular dissolution pores, and the main porosity is contributed by micropores (Table 3 and Figs. 7i and Fig. 8h).

The COPL values of the tightly compacted facies range from 30.4—33.8%, with an average of 31.3% (Table 3 and Fig. 9). The CEPL values range from 0.7—2.8%, with an average of 1.9% (Table 3 and Fig. 9). The tightly compacted facies, with the highest ductile grain content, are susceptible to ductile compaction, and catastrophic loss of intergranular porosity may occur during successive burial (Bjørlykke et al., 1989; Worden and Burley, 2003; Morad et al., 2010).

Table 3Diagenetic mineral and petrophysical data of the TGSs in the middle Permian Shihezi Formation.

Diagenetic facies	Well	Depth, m	Median grain size, um	Ductile grain, %	Quartz overgrowth, %	Calcite cement, %		Intergranular porosity, %	Intragranular dissolution porosity, %	Microp- orosity, %	So	OP	IGV	COPL	CEPL
Grain-coating facies	LD-17	1211.5 1212.3 1213.3 1233.0 1233.4 1359.7	404 408 367 545	3.0 4.0 3.0 1.0 2.0 3.0	0.0 0.0 0.0 0.0 0.0 0.0	0.0 0.0 0.0 0.0 0.0 0.0	3.0 2.0 3.0 2.0 4.0 3.0	7.0 6.0 7.0 11.0 10.0 7.0	6.0 4.0 7.0 4.0 5.0 5.0	4.3 4.2 3.7 2.6 2.2 2.9	3.7 3.6 2.8 4.2	27.1 27.2 29.0 26.4	8.0 10.0 13.0 14.0		2.4 1.6 2.4 1.6 3.4 2.4
Quartz-cemented facies	LD-17	1290.4 1297.5 1676.7 1511.7 1235.6 1236.4 1200.6	335 275 352 442 420	3.0 3.0 5.0 4.0 3.0 4.0 3.0	6.0 5.0 5.0 6.0 5.0 5.0 6.0	1.0 0.0 0.0 0.0 0.0 0.0 0.0	5.0 4.0 3.0 5.0 2.0 5.0 4.0	3.0 3.0 2.0 2.0 2.0 4.0 4.0	5.0 6.0 5.0 6.0 3.0 4.0 5.0	4.3 4.6 4.8 5.0 4.5 4.4 3.3	2.5 2.4 3.8 4.0 3.5	29.9 30.5 27.0 26.7 27.4	12.0 10.0 13.0 9.0 14.0	22.8 16.1 19.4 15.6	9.8 7.2 6.2 9.2 5.6 8.4 8.3
Mixed-cemented facies	LD-8 LD-8 LD-8 LD-8 LD-8 LD-8	1512.0 1512.6 1514.3 1514.8 1515.4 1516.2	259 253 226 305	6.0 8.0 8.0 7.0 7.0 6.0	6.0 3.0 6.0 4.0 3.0 4.0	1.0 1.0 1.0 3.0 9.0 10.0	4.0 6.0 6.0 5.0 3.0 7.0	0.0 0.0 0.0 0.0 0.0 0.0	7.0 6.0 4.0 4.0 6.0 5.0	5.3 7.2 5.0 4.0 4.8 5.0	3.2 2.9 2.9 3.0	28.9 28.7	10.0 13.0 12.0 15.0	20.0 18.2 19.0 16.1	9.0 8.0 10.6 9.7 12.6 18.4
Carbonate-cemented facies		1558.0 1559.7 1382.8 1737.5	320 252	5.0 5.0 5.0 4.0	0.0 0.0 0.0 0.0	20.0 21.0 20.0 22.0	1.0 2.0 1.0 1.0	0.0 0.0 0.0 0.0	2.0 0.0 1.0 2.0	2.8 5.1 4.8 1.5	2.1 3.3	32.4 31.8 27.9 32.1	23.0 21.0	11.4 8.7	18.0 20.4 19.2 20.3
Tightly compacted facies	LD-5 LD-5 LD-5 LD-5 LD-5	1588.6 1589.0 1589.4 1590.5 1653.2	199 284 272	13.0 14.0 12.0 13.0 14.0	0.0 0.0 0.0 0.0 0.0	2.0 2.0 1.0 0.0 3.0	1.0 2.0 1.0 1.0 1.0	0.0 0.0 0.0 0.0 0.0	1.0 0.0 1.0 0.0 0.0	4.0 4.9 4.0 5.8 5.4	1.7		4.0 2.0 1.0	30.4	2.1 2.8 1.4 0.7 2.8

5.2. Diagenetic facies and reservoir quality

Combining He porosity and permeability measurements and MICP and NMR measurements, we found that the grain-coating facies has the best pore structure and the greatest reservoir quality; the pore structure and reservoir quality of the quartz-cemented facies are poor compared to those of the grain-coating facies; the pore structure and reservoir quality of the mixed-cemented facies are relatively poor; and the pore structure and reservoir quality of the carbonate-cemented facies and tightly compacted facies are the worst (Table 4 and Figs. 10 and 11).

The maximum SHg/Pc ratio, known as the Swanson parameter (Swanson, 1981), coincides with the peak of the hyperbola on the log-log mercury injection plot. The rapex is the pore radius that corresponds to the Swanson parameter (Fig. 12a) (Swanson, 1981; Pittman, 1992; Nabawy et al., 2009). At this stage, the Swanson parameter implies that mercury has intruded into all connected spaces that govern permeability (Swanson, 1981; Comisky et al., 2007; Higgs et al., 2015). The change from a broad and wellconnected pore throat network to a narrow and poorly linked pore throat network is marked by the rapex in this curve (Fig. 12a) (Swanson, 1981; Pittman, 1992; Aliakbardoust and Rahimpour-Bona, 2013). A plot of the mercury saturation/injection pressure versus mercury saturation shows that a few relatively large pore throats contribute approximately 80% of the permeability in different diagenetic facies (Fig. 12). Compared with the relatively discrete correlation between porosity and permeability (Fig. 10), our analysis confirms that the permeability of the samples has a good positive correlation with the rapex (Fig. 12g). The permeability in TGSs is mainly contributed by a small fraction of large pore throats. The different pore types contribute differently to the permeability. Primary intergranular pores, which are joined by wider pore throats, contribute greatly to permeability (Bloch et al., 2002; Dutton and Loucks, 2010). Lower-permeability contributions are made by intragranular dissolution pores and intercrystalline micropores linked only by smaller pore throats (Midtbø et al., 2000; Bloch et al., 2002; Dutton and Loucks, 2010). In reality, feldspar dissolution causes the formation of authigenic quartz and authigenic minerals (Siebert et al., 1984; Bjørlykke et al., 1988; Worden and Burley, 2003). Because their crystallization habits and shapes effectively seal pore throats and do not contribute directly to fluid movement, the intercrystalline micropores in clay minerals are called dead-end pores (Lai et al., 2016; Mckinley et al., 2011; Samakinde et al., 2016).

In the grain-coating facies, the pore network is dominated by larger pore throats connecting primary intergranular pores (Fig. 7a and b), resulting in the maximum porosity and permeability of the facies (Fig. 10), as well as the best pore structure and reservoir quality (Fig. 11a-c). Petrographic observations and analysis of the pore structure indicate that quartz overgrowths lead to narrow, thin, lamellar, or trough-like pores, thereby diminishing the pore and pore throat diameters (Fig. 7c and d and Fig. 11d-f). Therefore, the reservoir quality of the quartz-cemented facies is inferior to that of the grain-coating facies (Fig. 10). High porosity does not always imply good permeability, and samples with high porosities but poor permeabilities can be found in mixed-cemented facies (Fig. 10). We suggest that the poor permeability of the mixedcemented facies is due to the increase in the ductile grain content and the various types of cementation (Fig. 8b-e), resulting in a large loss of intergranular porosity (Fig. 8f), with the pore space dominated by intragranular dissolution pores and intercrystalline micropores (Fig. 7e and f and Fig. 8g and h). In the carbonateZ.-Y. Wang, S.-F. Lu, N.-W. Zhou et al. Petroleum Science 21 (2024) 2946–2968

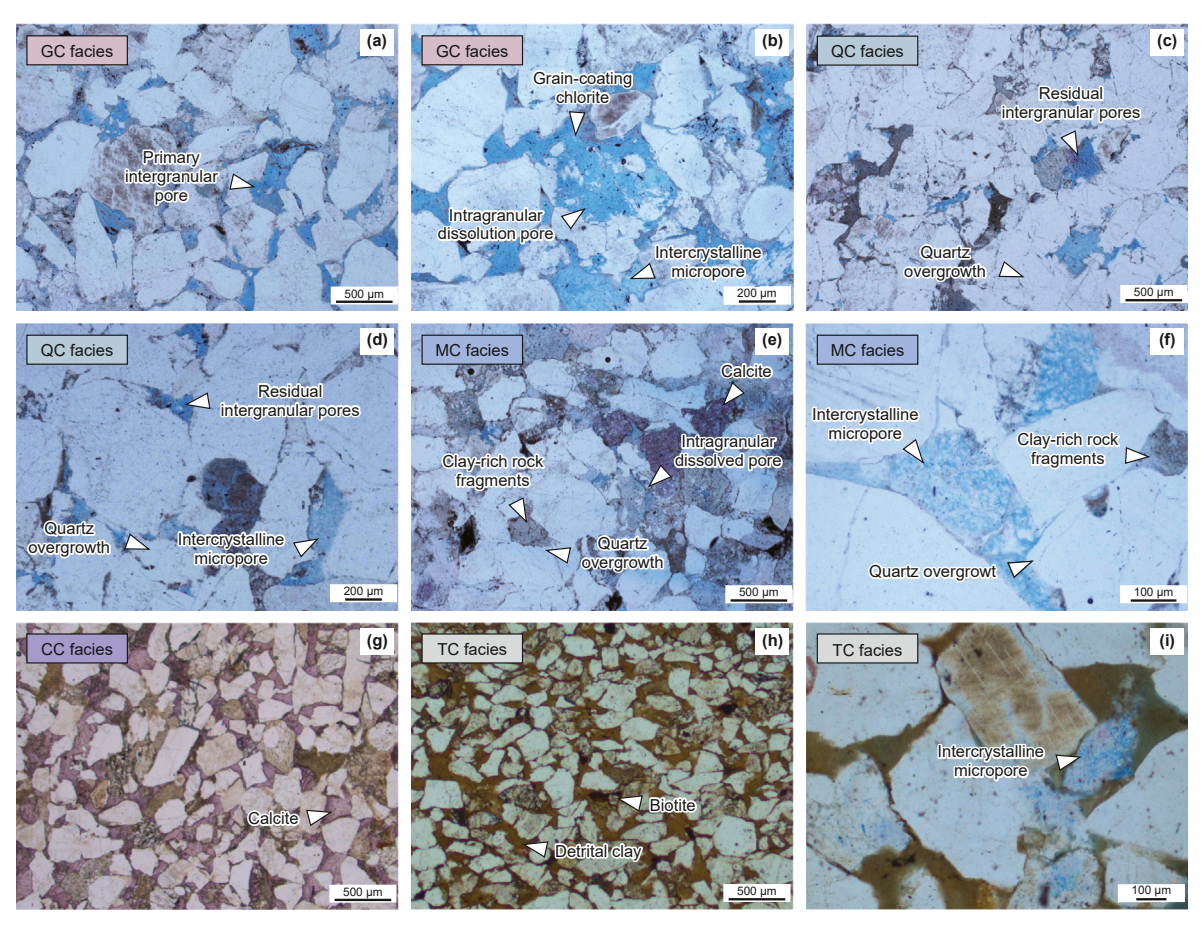


Fig. 7. Optical and SEM images of five types of diagenetic facies. (a) Grain-coating facies, Well LD-8, 1212.25 m, PPL; (b) grain-coating facies, Well LD-8, 1211.54 m, PPL; (c) quartz-cemented facies, Well LD-20, 1382.99 m, PPL; (d) quartz-cemented facies, Well LD-20, 1382.99 m, PPL; (e) mixed-cemented facies, Well LD-8, 1515.41 m, PPL; (f) mixed-cemented facies, Well LD-20, 1204.80 m, PPL; (g) carbonate-cemented facies, Well LD-13, 1737.48 m, PPL; (h) tightly compacted facies, Well LD-5, 1588.62 m, PPL; (i) tightly compacted facies, Well LD-5, 1590.5 m, PPL. GC facies = grain-coating facies, QC facies = quartz-cemented facies, MC facies = mixed-cemented facies, CC facies = carbonate-cemented facies, CC facies = tightly compacted facies.

cemented facies and tightly compacted facies, in which the intergranular pores are filled with carbonate cement and ductile grains (Fig. 7g—i), respectively, the pore network mainly consists of micropores (Fig. 8h), and the reservoir quality is the worst (Figs. 10 and 11j—o).

5.3. Diagenetic facies and gas productivity

Fig. 13 shows the gas productivity of the different diagenetic facies in the vertical well sections. Statistically, the vast majority of sections of grain-coating facies (89%) yield economic gas flow and do not require hydraulic fracturing (Fig. 13a). The maximum vertical well section productivity of the sections of grain-coating facies reaches 18.2×10^4 m³/d, and the average vertical well section productivity is 8.6×10^4 m³/d (Fig. 13b). In general, the quartzcemented facies section must be hydraulically fractured to yield economic gas flow. Most of the quartz-cemented facies sections (86%) fracture to yield economic gas flow (Fig. 13a). The highest vertical well section productivity is $7.6 \times 10^4 \, \text{m}^3/\text{d}$, and the average vertical well section productivity is 1.4×10^4 m³/d for the quartzcemented facies (Fig. 13b). Only a portion of the mixed-cemented facies sections (64%) yields economic gas flow after hydraulic fracturing (Fig. 13a). The maximum vertical well section productivity of mixed-cemented facies is only 1.0×10^4 m³/d, and the average vertical well section productivity is 0.5×10^4 m³/ d (Fig. 13b). None of the tightly compacted facies sections achieve

economic gas flow after hydraulic fracturing (Fig. 13).

Often, TGS production is correlated with reservoir quality and completion quality (Peters et al., 2016). Due to the low porosity and permeability, the tight sandstone gas closure mechanism is capillary closure rather than the mechanism of closure of conventional reservoirs, which is controlled by tectonics or stratigraphy. Higher-quality formations more easily form reservoirs because natural gas more easily breaks through the seal of the capillary force and enters traps (Meckel and Thomasson, 2008; Burnie et al., 2008). Poor reservoir quality may result in no natural gas injection and no production, even with high completion quality and effort. In other words, reservoir quality is the basis of the completion strategy and production, and it must be moderate to high for completion to be effective (Baihly et al., 2010; Ma et al., 2016). Therefore, poor quality formations with tightly compacted and carbonate-cemented facies are not targets for completion.

The rock brittleness of the target formation is a key parameter for gas release in hydraulic fracturing. A higher completion quality can be obtained when the brittleness of the section of the target formation is higher. More brittle rocks have higher brittleness index (BI) values. Rocks enriched in ductile clays affect the effectiveness of hydraulic fracturing, while those rich in silica, feldspar and relatively brittle calcite and dolomite have better geomechanical properties for tight reservoir production (Jarvie et al., 2007; Dong et al., 2017).

The grain-coating facies have the best reservoir quality (Fig. 10),

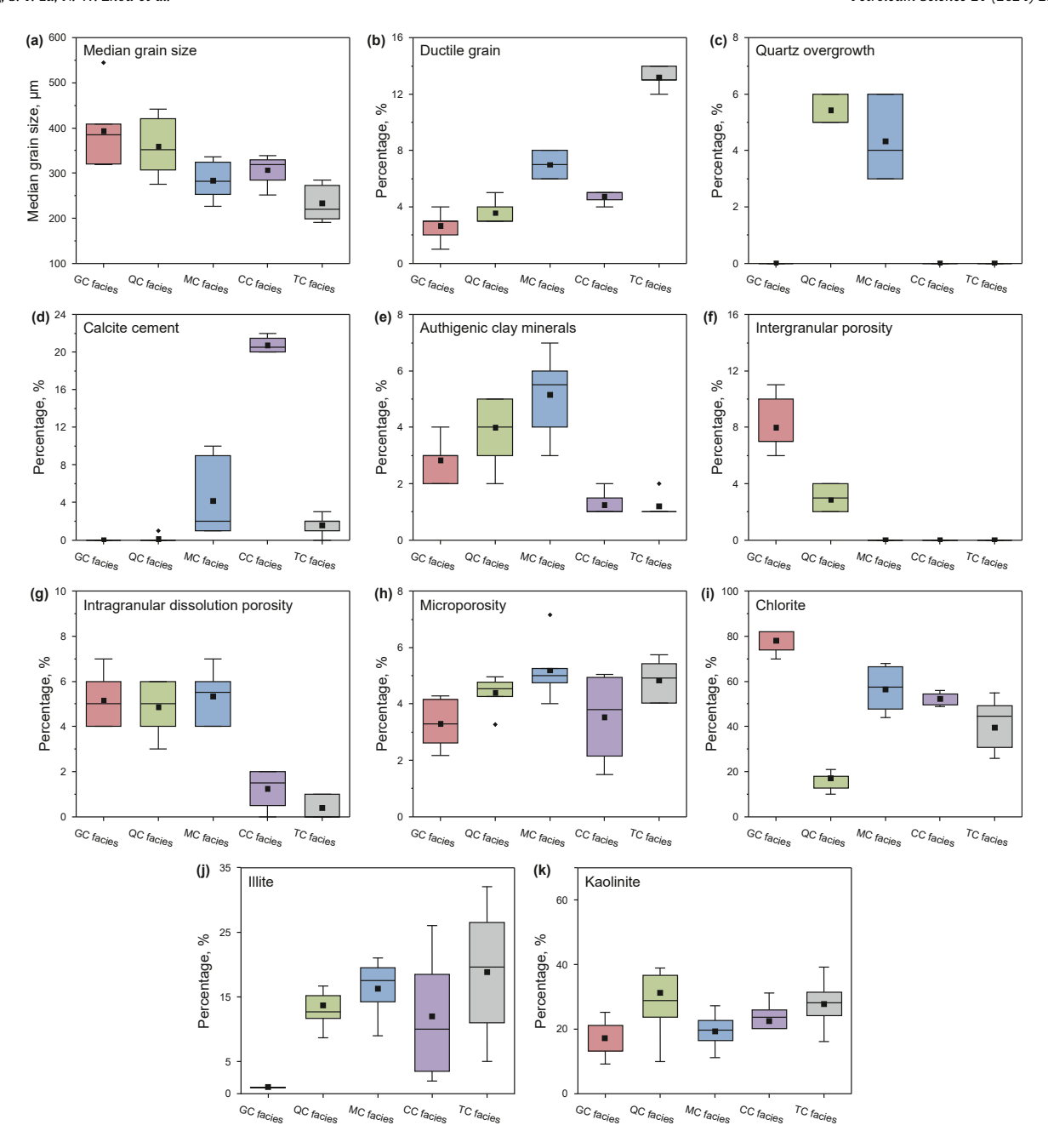


Fig. 8. (a) Median grain size, (b) ductile grain content via optical point counting, (c) quartz overgrowth content, (d) calcite cement content, (e) authigenic clay mineral content, (f) intergranular porosity, (g) intragranular dissolution porosity, (h) microporosity, (i) XRD pattern of chlorite, (j) XRD pattern of illite, and (k) XRD pattern of kaolinite for five types of diagenetic facies. GC facies = grain-coating facies, QC facies = quartz-cemented facies, MC facies = mixed-cemented facies, CC facies = carbonate-cemented facies, TC facies = tightly compacted facies.

even close to those of some conventional sandstone reservoirs, and therefore, they can yield economic gas flow without hydraulic fracturing (Fig. 13). Quartz-cemented formations also have better reservoir quality (Fig. 10) and the highest rock brittleness due to the high quartz and low clay contents (Table 5), and the gas productivity of the vertical well section is second only to that of the sections of grain-coating facies (Fig. 13). The higher ductile grain contents in the mixed-cemented facies not only lead to poor reservoir quality (Fig. 10) but also to realistic poor rock brittleness (Table 5); this is not conducive to the release of gas after hydraulic fracturing, resulting in lower productivity (Fig. 13).

5.4. Wireline log responses of diagenetic facies

We analyzed the correlation between diagenetic facies and wireline logs. Where severe water—rock interactions are present and where sandstones acutely pinch out to mudstones, carbonate-cemented facies typically occur at the edges of sandstones (Morad et al., 2010; Loyd et al., 2012). Typical carbonate-cemented facies have a thin vertical distribution and are not gas-producing formations due to their tight nature; therefore, no separate correlation analysis of wireline logs has been performed on carbonate-cemented facies.

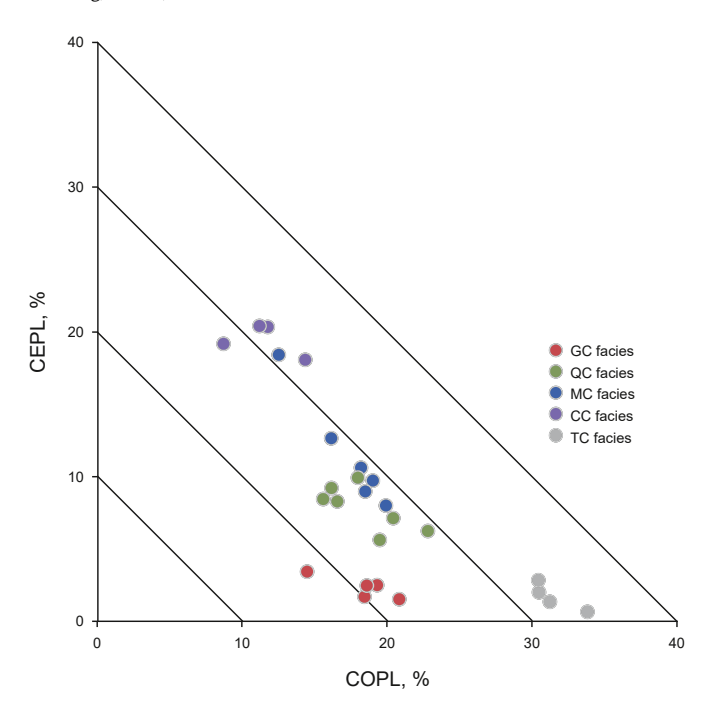


Fig. 9. Cemented porosity loss (CEPL) and compaction porosity loss (COPL) for various diagenetic facies. After Lundegard (1992). GC facies = grain-coating facies, QC facies = quartz-cemented facies, MC facies = mixed-cemented facies, CC facies = carbonate-cemented facies, TC facies = tightly compacted facies.

5.4.1. Wireline log responses of grain-coating facies

The grain-coating facies is considered to have low GR values, as well as low DEN, low CNL, low RT, and high AC values in wireline logs (Figs. 14a—15a and 16).

Theoretically, because grain-coating facies have the lowest clay content (Fig. 8b and e), they have little impact on the gamma-ray log. Therefore, grain-coating facies usually have low GR values (Figs. 14a–15a and 16a).

Since chlorite has a high density (Table 6), sandstones that are chlorite-enriched may have somewhat higher DEN values than sandstones that are chlorite-free because the matrix density is greater. However, this may not be largely detectable on a suite of log responses since only as much as 3 or 4% chlorite may cover all sand grain surfaces. An increase in the porosity starting from a porosity that prevents quartz cement development would result in a low DEN value, and this difference may mask the effect of the higher grain density (Figs. 14a–15a and 16c).

The compressional AC values of chlorite are not especially well

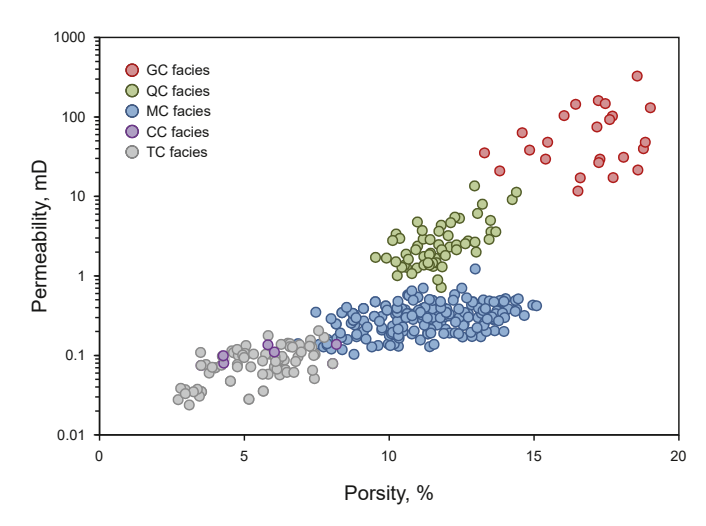


Fig. 10. Plot of the porosity versus permeability for various diagenetic facies in cores. GC facies = grain-coating facies, QC facies = quartz-cemented facies, MC facies = mixed-cemented facies, CC facies = carbonate-cemented facies, TC facies = tightly compacted facies.

defined but can be assumed to be similar to those of other clay minerals and slightly greater than those of framework minerals, such as quartz (Rider and Kennedy, 2011). The AC response recorded by the DEN log and the additional porosity that results from the prevention of quartz cement growths lead to high overall AC values (Figs. 14a—15a and 16b).

In contrast to chlorite, which has eight hydrogen atoms for every 20 oxygen atoms, illite has only two hydrogen atoms for every 20 oxygen atoms. As a result of the high number of hydrogen atoms present in each unit cell, chlorite exhibits a noticeable neutron reaction (Table 6). Although the increased porosity caused by the suppression of quartz cement results in a noticeable neutron response, the presence of chlorite results in a relatively high CNL reaction because of the excess hydrogen in the chlorite (Figs. 14a–15a and 16e).

The low RT response is a consequence of the microporous grain-coating chlorite, which enables water to be trapped inside the clay network (Fig. 5m), even after gas filling (Pratama et al., 2017, Figs. 14a–15a and 16d).

Similar to the laboratory core test data, the typical T₂ spectra from NMR logging can show either a bimodal or unimodal distribution, with the left peak typically corresponding to small pores, while the right peak is associated with larger pores (Solanet et al., 1998; Jacobsen et al., 2006; Freedman, 2006). Thus, high-

Table 4Pore structure and reservoir quality features for various diagenetic facies.

Diagenetic facies	Porosity	Permeability, mD	MICP pore throat connectivity	NMR T ₂ spectrum
Grain-coating facies	15-20%	10-160	The highest SHgmax with very low displacement pressure implies the presence of large, linked pore throats. The main pore throat radii range from $0.1-10~\mu m$.	The NMR T ₂ relaxation distribution is bimodal. The presence of large T ₂ relaxation times (>100 ms) demonstrates that a high percentage of large pores are retained.
Quartz-cemented facies	9-15%	0.8-11	The SHgmax is high, and the driving pressure has a low discharge. The main pore throat radii range from $0.06-6~\mu m$.	The NMR T_2 relaxation distribution is bimodal. A large T_2 relaxation time (>100 ms) is present.
Mixed-cemented facies	7–15%	0.4-1.2	The SHgmax is lower, and the displacement pressure is greater. The main pore throat radii range from 0.04–4 $\mu m.$	The NMR T_2 relaxation distribution is unimodal. The proportion of large T_2 relaxation times (>100 ms) is low, which indicates that a low proportion of large pores are retained.
Carbonate-cemented facies and tightly compacted facies	4.2-6.8%	0.02-0.08	The SHgmax is very low, and the displacement pressure is high. The main pore throat radii range from 0.01–1 $\mu m.$	The NMR T_2 relaxation distribution is unimodal. The NMR T_2 relaxation range of $1.0-3$ ms, suggests that small pores dominate the pore network.

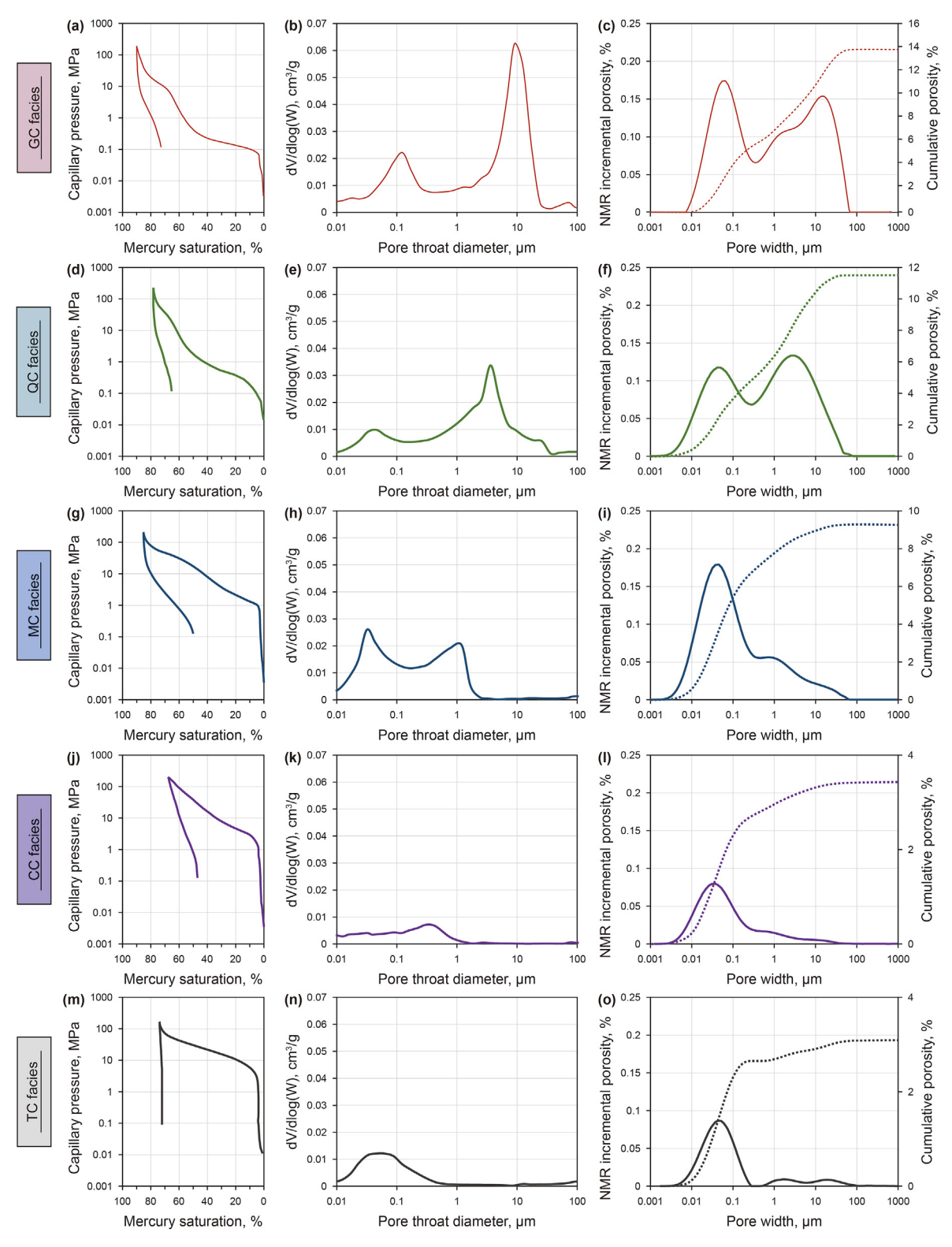


Fig. 11. (a, d, g, j, m) Mercury intrusion and extrusion curves, (b, e, h, k, n) pore throat size distribution revealed by MICP, and (c, f, i, l, o) NMR T₂ distributions for various diagenetic facies. GC facies = grain-coating facies, QC facies = quartz-cemented facies, MC facies = mixed-cemented facies, CC facies = carbonate-cemented facies, and TC facies = tightly compacted facies.

reservoir-quality formations are those with broad NMR T₂ spectra distributions and high right peaks. The pore network of the grain-coating facies is dominated by larger primary intergranular pores (Fig. 8g); therefore, a very wide distribution of NMR T₂ spectra and

a very high right peak are observed (Fig. 14a).

5.4.2. Wireline log responses of the quartz-cemented facies
The quartz-cemented facies wireline log responses show low GR

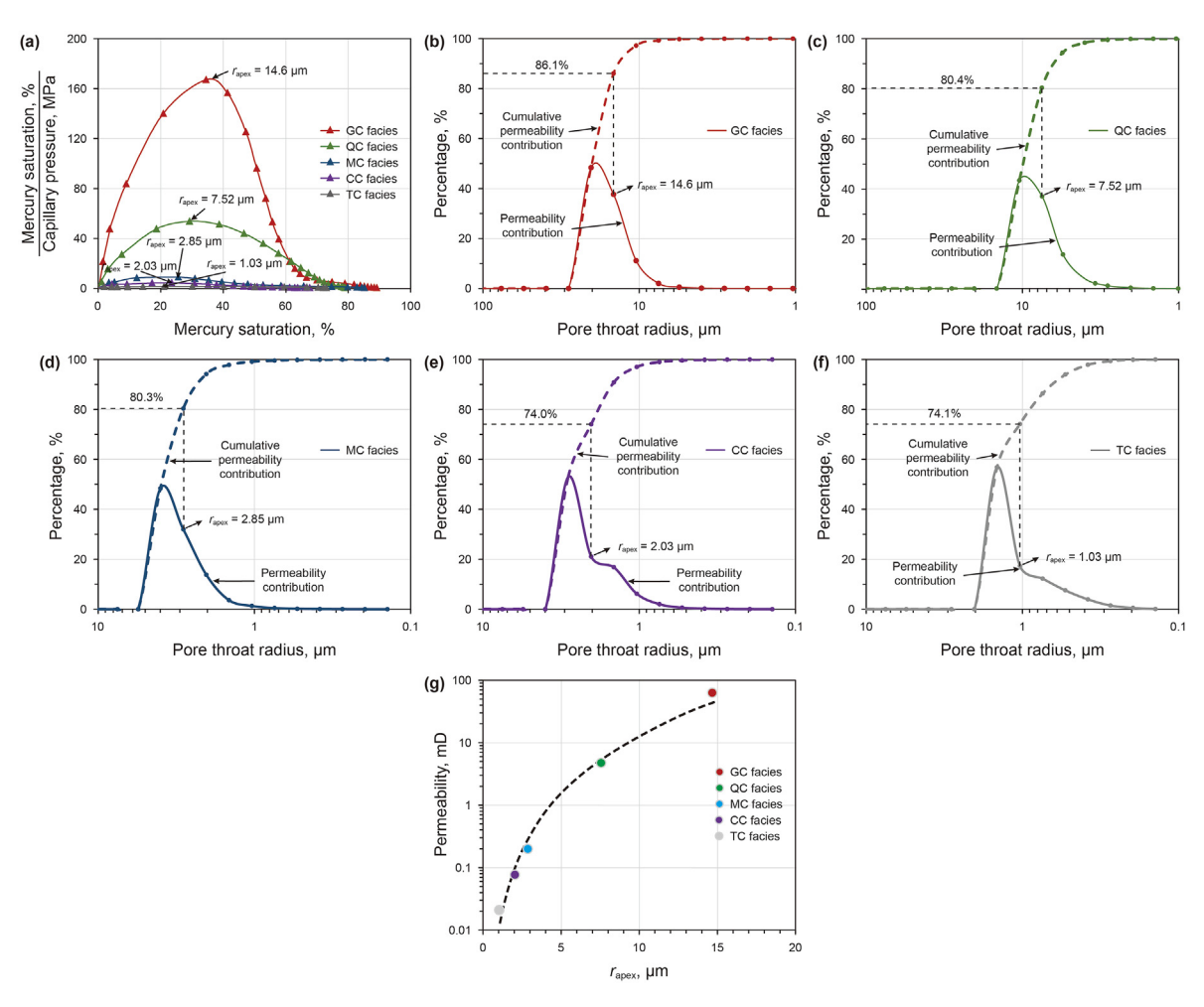


Fig. 12. (a) Plot of the mercury saturation/injection pressure versus mercury saturation; (b—f) contributions of different pore throat sizes of various diagenetic facies to permeability; (g) relationship between the rapex and permeability of various diagenetic facies. GC facies = grain-coating facies, QC facies = quartz-cemented facies, MC facies = mixed-cemented facies, CC facies = carbonate-cemented facies, TC facies = tightly compacted facies.

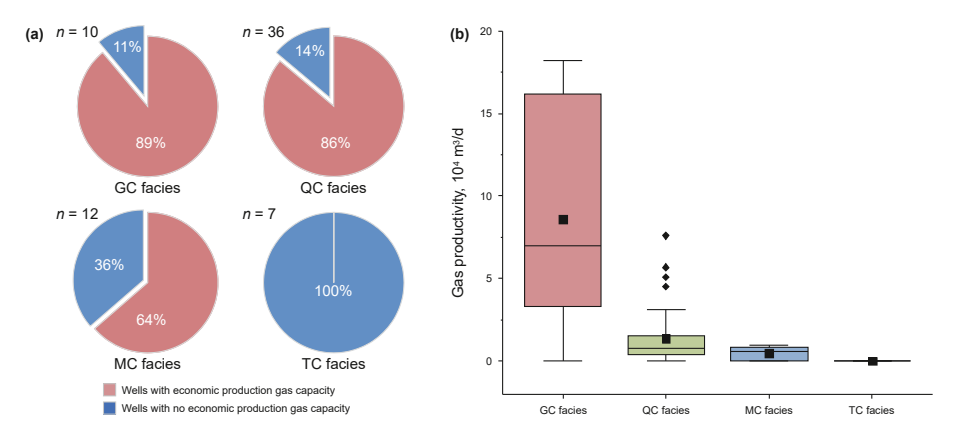


Fig. 13. (a) Percentage of economic production capacity and noneconomic production capacity and **(b)** vertical well section productivity for various diagenetic facies. GC facies = grain-coating facies, QC facies = quartz-cemented facies, MC facies = mixed-cemented facies, CC facies = carbonate-cemented facies, CC facies = tightly compacted facies. n = number of samples.

values, low to medium DEN and medium to high CNL and AC values (Figs. 14b-15b and 16), as well as a medium-width NMR logging T_2 spectrum distribution with a leftward shift of the T_2 spectrum (Fig. 14b).

The GR values of the quartz-cemented facies are usually slightly

greater than those of the grain-coating facies (Fig. 16a). The clay in the quartz-cemented facies has a greater illite content (Fig. 8j), which results in both neutron and gamma responses (Table 6). The porosity loss that results from quartz cement growth in the quartz-cemented facies leads to lower overall AC values and higher DEN

Table 5Brittleness index (BI) for various diagenetic facies.

Diagenetic facies	Wells	Depth, m	σ_c , MPa	σ_{d} , MPa	BI
Grain-coating facies	LD-8	1211.4	25.1	2.4	10.6
Quartz-cemented facies	LD-20	1380.4	35.5	3.4	10.6
Mixed-cemented facies	LD-3	1512.4	49.9	5.9	8.5
Tightly compacted facies	LD-1	1385.2	62.0	15.4	4.0

The brittleness index is BI = σ_c/σ_d , where σ_c is the compressive strength and σ_d is the tensile strength (Aubertin et al., 1994; Ribacchi, 2000).

values than those in the grain-coating facies (Figs. 14b-15b and 16b and c). The quartz-cemented facies have a medium-width NMR logging T_2 spectrum with a leftward shift in the T_2 spectrum due to

the deterioration of the pore structure caused by the loss of large intergranular pores (Fig. 14b).

5.4.3. Wireline log responses of mixed-cemented facies

The mixed-cemented facies has medium to high GR and CNL values, medium to high DEN values, and medium to low AC values (Figs. 14c–15c and 16).

The high GR values of mixed-cemented facies are due to their possible inclusion of more highly radioactive clay-rich rock fragments, as well as a clay matrix (Fig. 7e and f and Fig. 8b). Localized precipitation of quartz, carbonate cement, and authigenic clay minerals (Fig. 8b—e) results in a low bulk density, leading to relatively high CNL, medium to low AC and medium to high DEN values

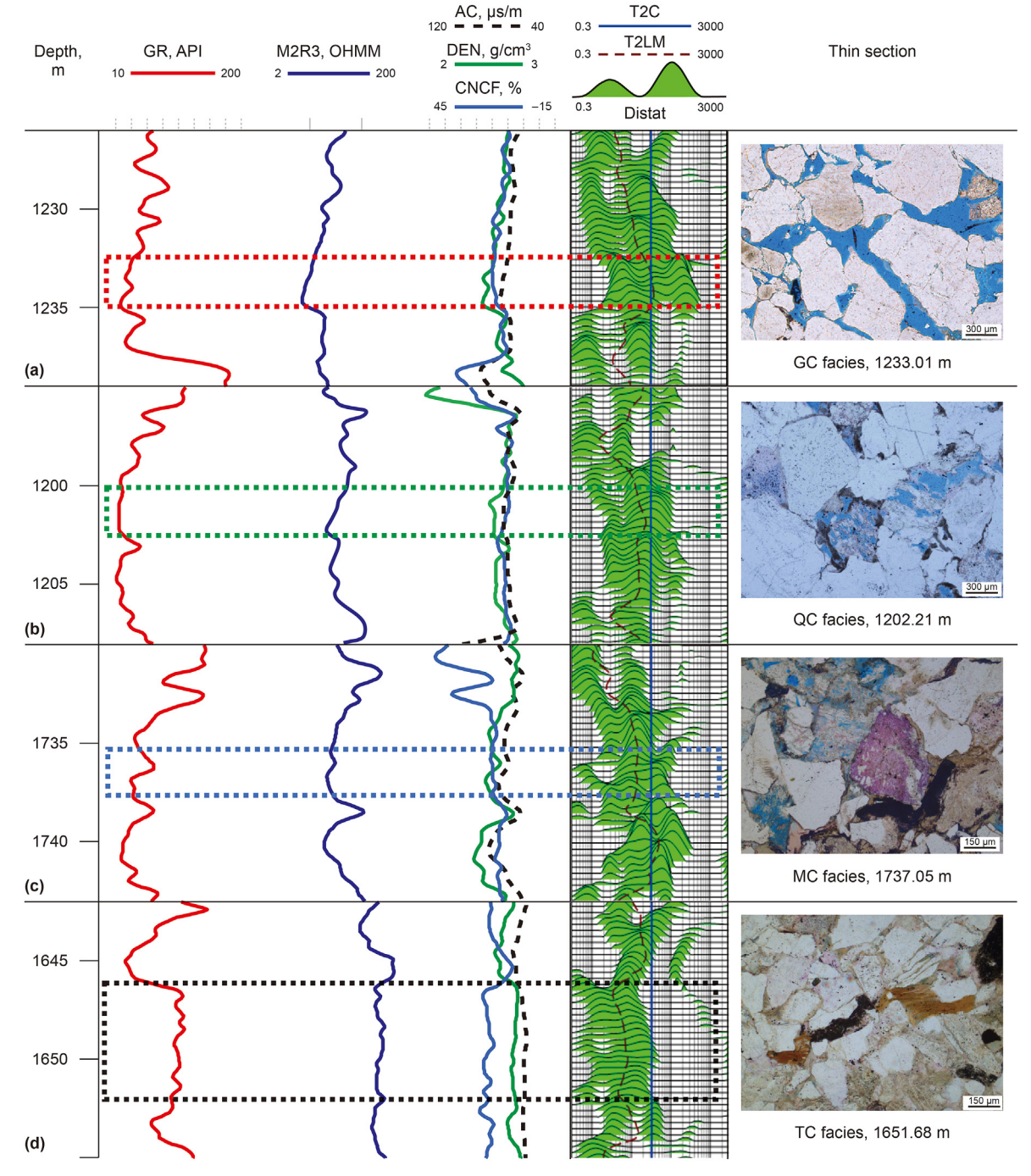


Fig. 14. Wireline log responses showing the various diagenetic facies. (a) Grain-coating facies. (b) Quartz-cemented facies. (c) Mixed-cemented facies. (d) Tightly compacted facies.

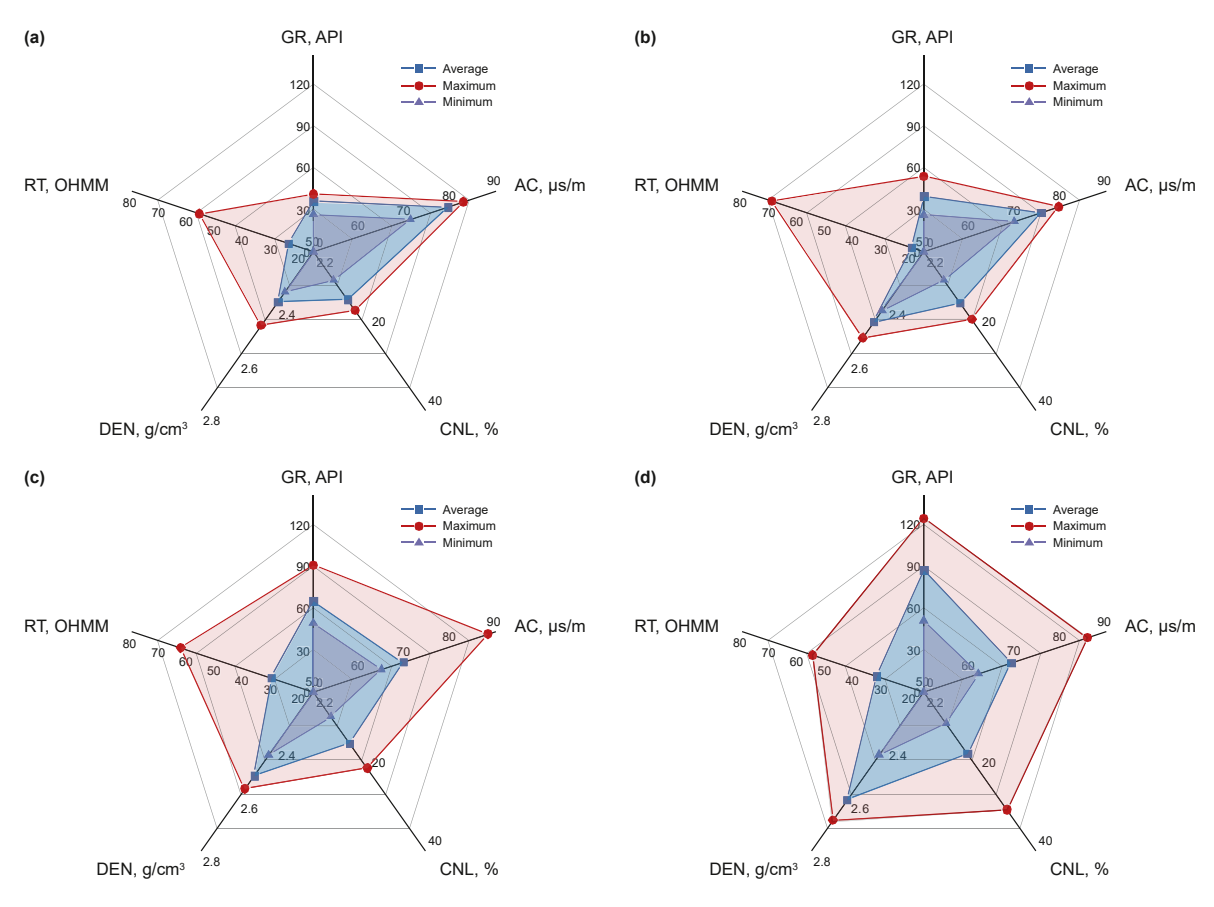


Fig. 15. Radar chart of the wireline log responses of various diagenetic facies. (a) Grain-coating facies. (b) Quartz-cemented facies. (c) Mixed-cemented facies. (d) Tightly compacted facies.

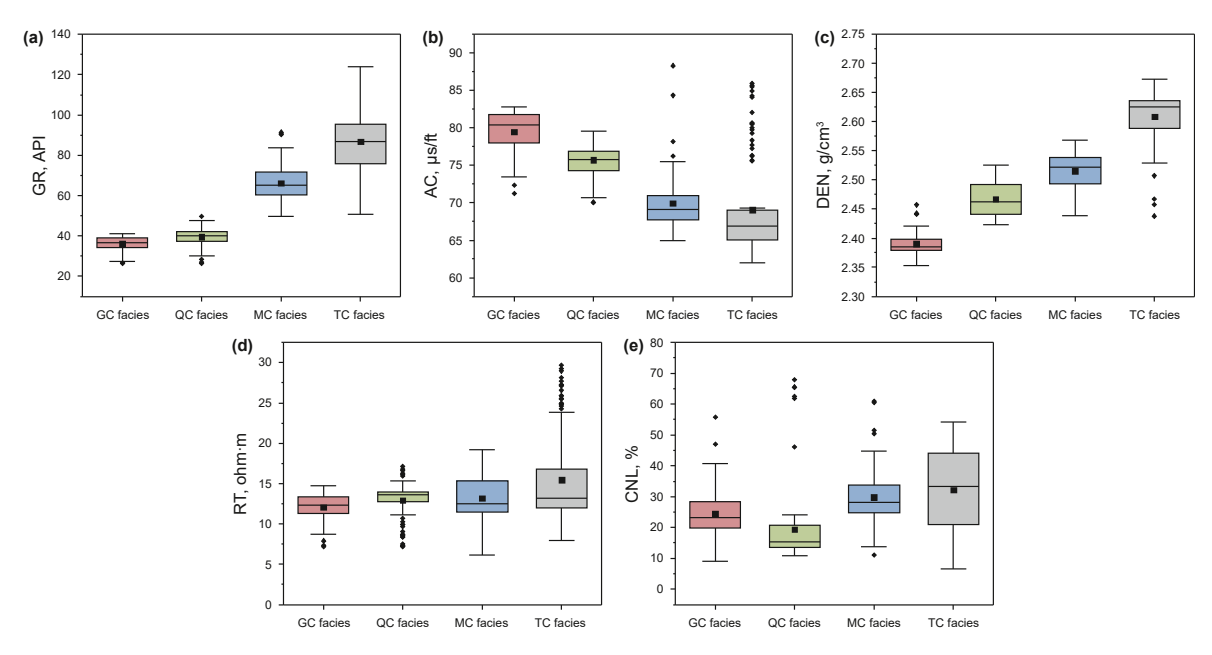


Fig. 16. Diagenetic facies distribution in wireline logs. (a) Gamma ray (GR) wireline logs, (b) acoustic transit time (AC) wireline logs, (c) bulk density (DEN) wireline logs, (d) resistivity (RT) wireline logs, and (e) compensated neutron (CNL) wireline logs.

(Fig. 16b, c and e). The microporous-rich mixed-cemented facies have low total porosity, a poorer pore structure, and a medium-

width NMR logging T_2 spectrum distribution, with a leftward shift in the T_2 spectrum (Fig. 14c).

Table 6Readings of well logging characteristics of common rock-forming minerals (from Schön, 2015).

Minerals	$\rho_{\rm b}$, g/cm ³	$\rho_{\rm log}$, g/cm ³	φ _{CNL} , %	$\Delta t_{\rm p}$, μs/m	$\Delta t_{\rm s}$, $\mu {\rm s/m}$	∑, c.u.	GR, API	Th, ppm	U, ppm	К, %
Quartz	2.65	2.64	-2	51	74	4.3		2.0	0.7	0.0
K-feldspar	2.56	2.53	-3	69		16.0	-220	8-12		10.5-16.0
Albite	2.62	2.59	-2	49	85	7.5				
Calcite	2.71	2.71	0	46	89	7.1				0 - 7.0
Kaolinite	2.59	2.62	37	212	328	14.0	80-130	6-19	4.4 - 7.0	0-0.5
Chlorite	2.88	2.88	52			25.3	180-250	0-8	17.4-36.2	0-0.3
Illite	2.64	2.63	30			18.0	250-300	10-25	8.7 - 12.4	3.5-8.3
Montmorill-onite	2.06	2.02	60			14.0	150-200	14-24	4.3 - 7.7	0-1.5
Muscovite	2.83	2.82	20	47	79	16.9	-270	20-25	2.0 - 8.0	7.8 - 9.8
Biotite	3.01	2.99	21	51	224	30.0	200-360	5-50	1.0-40	5.2-10
Pyrite	5.01	5	-3	38	59	89.8	200-350	5-50	1.0 - 40.0	6.2 - 10.0

 $\rho_{\rm b}=$ bulk density; $\rho_{\rm log}=$ log density (gamma–gamma density); $\varphi_{\rm CNL}=$ CNL value; $\Delta t_{\rm p}=$ slowness for the compressional wave; $\Delta t_{\rm s}=$ slowness for the shear wave; $\Sigma=$ macroscopic cross-section of the units in the analysis.

5.4.4. Wireline log responses of tightly compacted facies

The wireline log response of the tightly compacted facies is characterized by high GR and CNL values, high DEN and RT values and low AC values (Figs. 14d—15d and 16).

The high GR response of tightly compacted facies is due to the large amount of highly radioactive clay matrix and clay-rich rock fragments filling the pore spaces (Fig. 7h and i and Fig. 8b). The catastrophic loss of porosity due to strong compaction leads to low AC and high CNL and DEN values (Figs. 14d—15d and 16b, c and e).

The tightly compacted facies has a high RT response because almost all the pore spaces are filled with a clay matrix and clay-rich rock fragments, and a low water content is present. The pore network of the tightly compacted facies is dominated by micropores, and the pore structure is the worst, so the NMR T_2 spectrum is distributed near the left boundary and has a very low right peak height (Fig. 14d).

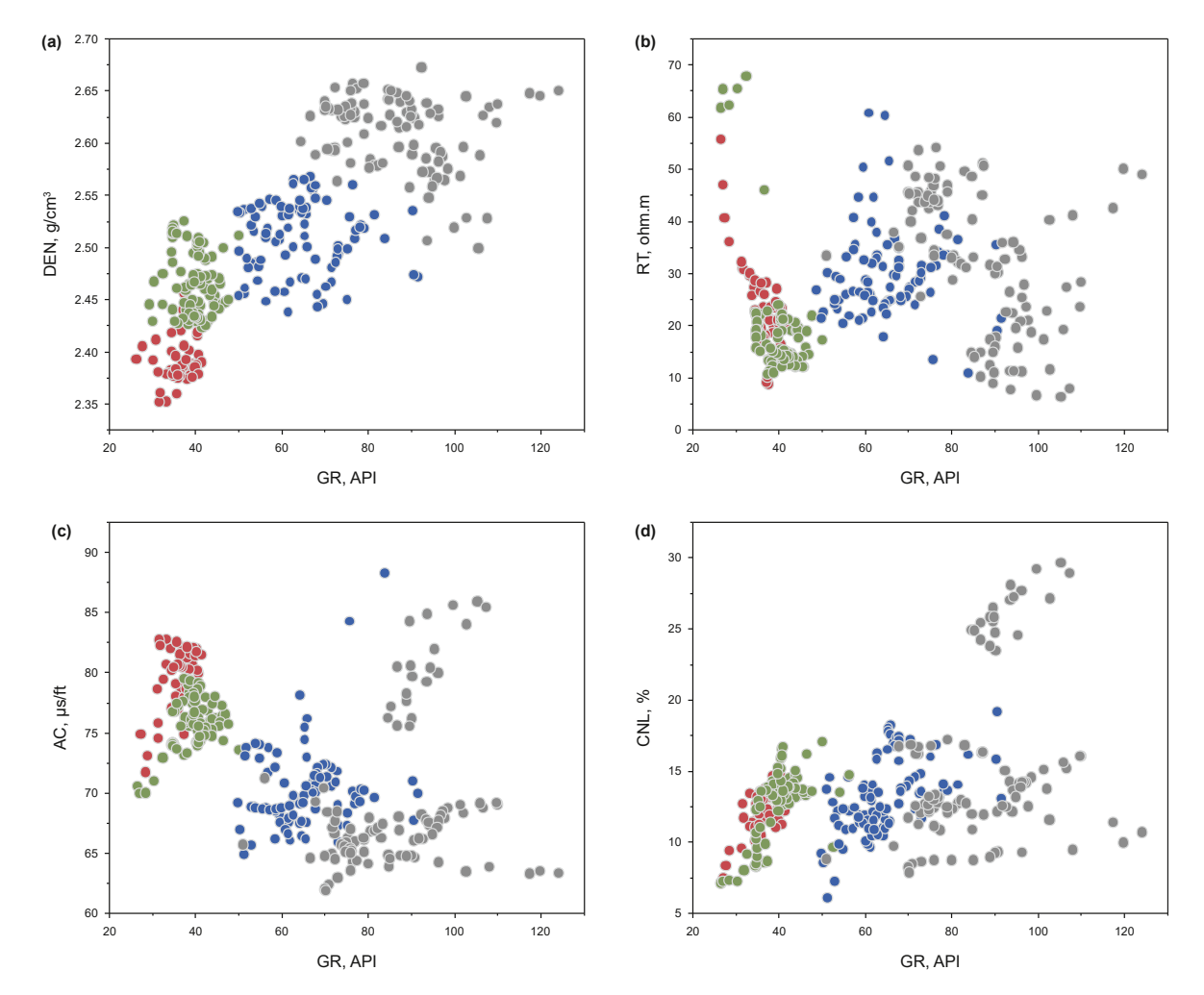


Fig. 17. Diagenetic facies distribution in wireline log cross-plots. (a) Gamma ray (GR) and bulk density (DEN) wireline logs, (b) gamma ray (GR) and resistivity (RT) wireline logs, (c) gamma ray (GR) and acoustic transit (AC) time wireline logs, and (d) gamma ray (GR) and compensated neutron (CNL) wireline logs.

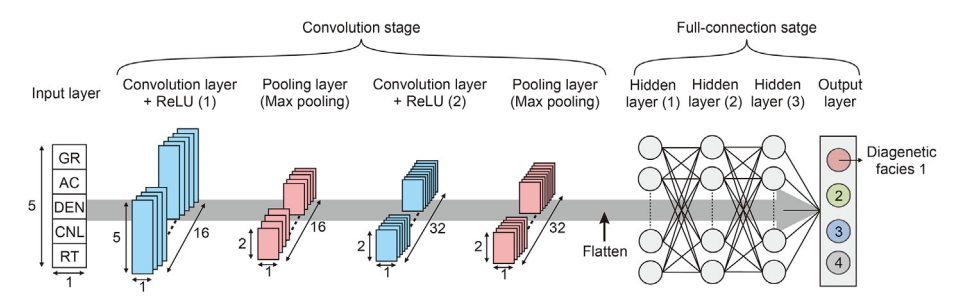


Fig. 18. Final CNN model structure.

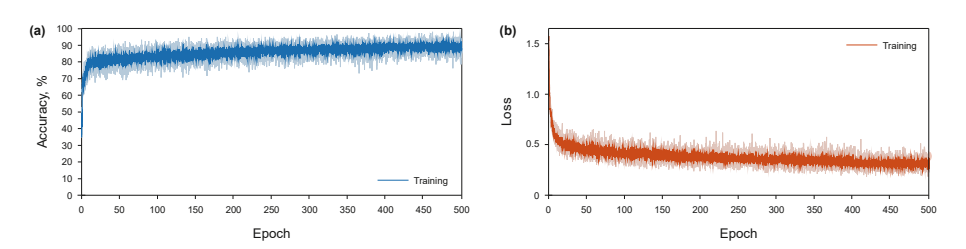


Fig. 19. (a) Accuracy and (b) loss of the CNN model over increasing epochs.

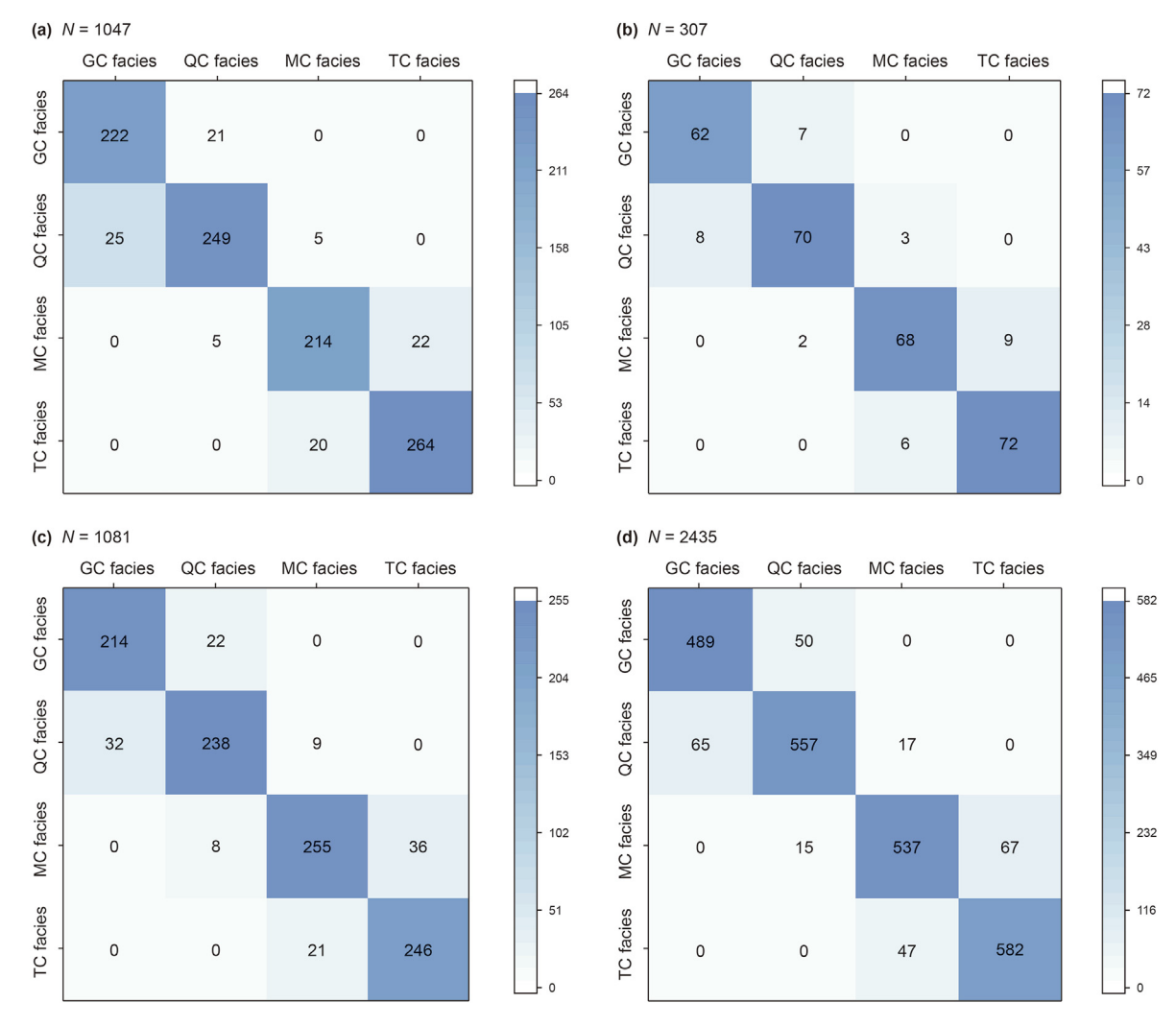


Fig. 20. Unnormalized confusion matrix highlighting how many diagenetic facies are correctly or incorrectly predicted. (a) Training data, (b) validation data, (c) test data, and (d) all data.

Table 7 Model accuracy comparison.

Model	Accuracy			
	Training	Validation	Test	All
CNN	90.6%	88.6%	88.3%	89.3%
ANN	87.4%	84.2%	83.6%	84.7%
RF	85.3%	82.2%	81.7%	82.6%

5.5. Diagenetic facies predictions utilizing a convolutional neural network

Due to the highly overlapping characteristics between each

diagenetic facies, it is not possible to distinguish diagenetic facies when using a single wireline log (Fig. 16). The wireline log values of the various diagenetic facies still overlap when interacting with two single wireline logs (Fig. 17), making it exceedingly challenging to forecast diagenetic facies.

A convolutional neural network (CNN) model was utilized for diagenetic facies prediction. Hyperparameters were selected using a random search, followed by 5-fold cross-validation on the training data. The parameters for the final model are detailed in Table S3. This model was optimized with these parameters (Fig. 18) and was designed to iterate for up to 500 epochs to minimize loss. Initially, the loss decreased rapidly within the first 25 epochs, after which the rate of decrease slowed (Fig. 19).

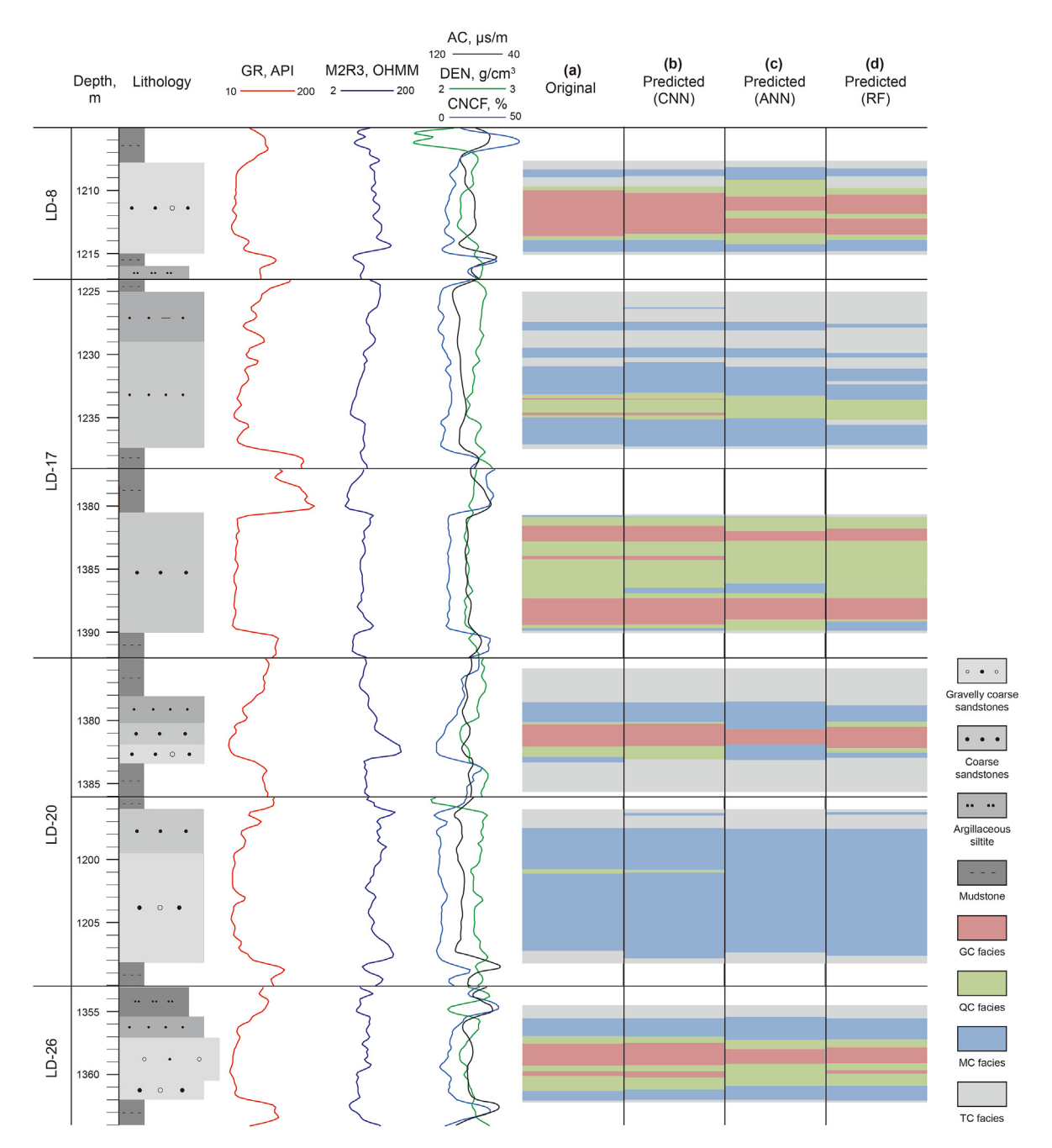


Fig. 21. Wireline logs and diagenetic facies of Wells LD-8, LD-17, LD-20 and LD-26. (a) Original diagenetic facies (core-interpreted). (b) Diagenetic facies predicted by the CNN model. (c) Diagenetic facies predicted by the ANN model. (d) Diagenetic facies predicted by the RF model.

Subsequently, a machine learning model based on a CNN model was evaluated for diagenetic facies prediction. The performance details are presented in the confusion matrices in Fig. 20. The results show that the total percentage of correct data in the training set is 90.6%, the total percentage of correct data in the validation set is 88.6%, the total percentage of correct data in the test set is 88.3%, and the total percentage of correct data in the training set is 89.3% (Table 7).

The CNN model's performance was benchmarked against that of the ANN model, which consists of fully connected layers and mirrors the full-connection stage of the CNN model used in this study. The ANN model shares the same structure as the fully connected stage (three hidden layers) of the final CNN model used in this study. Additionally, a fully optimized random forest (RF) model was considered (Fig. S1). The accuracy comparisons revealed that the CNN model consistently outperformed the ANN model by approximately 3–5% across all four datasets (training, validation, test, and overall), as shown in Table 7. Compared to the RF model, the CNN model demonstrated greater accuracy for all datasets (Table 7).

Fig. 21 shows a visual comparison between the diagenetic facies based on core interpretation and the diagenetic facies predicted by the CNN model. The predicted diagenetic facies reproduced the stacking patterns, similar to the diagenetic facies of the original core interpretation. Although diagenetic facies are challenging to categorize in traditional wireline crossplots because of the overlapping of eigenvalues, the CNN model can be used to identify criteria for diagenetic facies classification through extensive mathematical calculations based on local filtering and logical networks. Although the ANN and RF models can be used to distinguish different diagenetic facies, their performances are notably inferior to those of the CNN model, especially in identifying grain-coating and quartz-cemented facies (Fig. 21). Accurate prediction of commercially valuable "sweet spots" is crucial for TGS reservoir exploration and development (Hood and Yurewicz, 2008; Xiao et al., 2017; Wang et al., 2023a, 2023b). The grain-coating and quartz-cemented facies in the Shihezi Formation are identified as the most promising "sweet spots." Thus, the CNN model's superior accuracy in predicting these facies highlights its statistical advantage and practical application in pinpointing "sweet spots" more precisely than the ANN and RF models.

6. Conclusions

- (1) Five diagenetic facies categories based on the detrital composition, diagenetic minerals and pore type assemblages are defined: grain-coating facies, quartz-cemented facies, mixed-cemented facies, carbonate-cemented facies, and tightly compacted facies.
- (2) Grain-coating facies with chlorite coatings that inhibit quartz overgrowths and large intergranular pores that dominate the pore network have the best reservoir quality. Quartz-cemented facies exhibit strong quartz overgrowths, resulting in the deterioration of reservoir quality. In mixed-cemented facies, the cementation of various authigenic minerals increases the abundance of micropores, resulting in poor reservoir quality. Carbonate-cemented facies and tightly compacted facies, in which the intergranular pores are filled with carbonate cement and ductile grains, respectively, have the worst reservoir quality.
- (3) Grain-coating facies with good reservoir properties are more likely to have high gas productivity and are the primary targets for exploration and development. The gas productivity of the quartz-cemented facies is second only to that of the grain-coating facies. A mixed-cemented facies with poorer reservoir quality results in lower gas productivity.

- Carbonate-cemented facies and tightly compacted facies, which have the worst reservoir quality, are not targets for well completion.
- (4) For distinct diagenetic facies, different wireline log combinations have different response characteristics. The prediction model based on the CNN machine learning algorithm and wireline log data can accurately classify the diagenetic facies of deeply buried TGSs.

CRediT authorship contribution statement

Zi-Yi Wang: Writing — review & editing, Writing — original draft, Validation, Supervision, Software, Resources, Project administration, Methodology, Investigation, Formal analysis, Data curation. **Shuang-Fang Lu:** Investigation, Funding acquisition. **Neng-Wu Zhou:** Data curation. **Yan-Cheng Liu:** Data curation. **Li-Ming Lin:** Data curation. **Ya-Xin Shang:** Software. **Jun Wang:** Software. **Guang-Shun Xiao:** Software.

Declaration of competing interest

The authors declare that they have no known competing financial interests or personal relationships that could have appeared to influence the work reported in this paper.

Acknowledgments

This work was financially supported by the National Natural Science Foundation of China (No. 42272156) and research on efficient exploration and development technology for tight stone gas of China United Coalbed Methane Corporation (No. ZZGSECCYWG 2021-322). We thank Hamzeh Mehrabi, PhD and seven other anonymous reviewers for their thorough and critical reviews and suggestions, which greatly improved the manuscript.

Appendix A. Supplementary data

Supplementary data to this article can be found online at https://doi.org/10.1016/j.petsci.2024.08.008.

References

- Ajdukiewicz, J.M., Lander, R.H., 2010. Sandstone reservoir quality prediction: the state of the art. AAPG Bull. 94 (8), 1083–1091. https://doi.org/10.1306/intro060110.
- Al Khalifah, H., Glover, P.W.J., Lorinczi, P., 2020. Permeability prediction and diagenesis in tight carbonates using machine learning techniques. Mar. Petrol. Geol. 112, 104096. https://doi.org/10.1016/j.marpetgeo.2019.104096.
- Aliakbardoust, E., Rahimpour-Bonab, H., 2013. Effects of pore geometry and rock properties on water saturation of a carbonate reservoir. J. Petrol. Sci. Eng. 112, 296–309. https://doi.org/10.1016/j.petrol.2013.11.018.
- Antariksa, G., Muammar, R., Lee, J., 2022. Performance evaluation of machine learning-based classification with rock-physics analysis of geological lithofacies in Tarakan Basin, Indonesia. J. Petrol. Sci. Eng. 208, 109250. https://doi.org/ 10.1016/j.petrol.2021.109250.
- Aubertin, M., Gill, D.E., Simon, R., 1994. On the use of the brittleness index modified (BIM) to estimate the post-peak behavior of rocks. In: ARMA North America Rock Mechanics Symposium (pp. ARMA-1994). ARMA.
- Aversana, P., 2019. Comparison of different Machine Learning algorithms for lith-ofacies classification from well logs. Boll. Geofis. Teor. Appl. 60 (1). https://doi.org/10.4430/bgta0256.
- Bahrehvar, M., Mehrabi, H., Akbarzadeh, S., Rahimpour-Bonab, H., 2021. Depositional and diagenetic controls on reservoir quality of the uppermost Jurassic-Lower Cretaceous sequences in the Persian Gulf; a focus on J–K boundary. J. Petrol. Sci. Eng. 201, 108512. https://doi.org/10.1016/j.petrol.2021.108512.
- Baihly, J.D., Malpani, R., Edwards, C., Han, S.Y., Kok, J.C., Tollefsen, E.M., Wheeler, C.W., 2010. Unlocking the shale mystery: how lateral measurements and well placement impact completions and resultant production. In: SPE Unconventional Resources Conference/Gas Technology Symposium. SPE,

- pp. SPE-138427. https://doi.org/10.2118/138427-MS.
- Beard, D.C., Weyl, P.K., 1973. Influence of texture on porosity and permeability of unconsolidated sand. AAPG Bull. 57 (2), 349–369. https://doi.org/10.1306/ 819A4272-16C5-11D7-8645000102C1865D.
- Bjørlykke, K., 1988. Sandstone diagenesis in relation to preservation, destruction and creation of porosity. Dev. Sedimentol. 41, 555–588. https://doi.org/10.1016/ S0070-4571(08)70180-8. Elsevier, 1988.
- Bjørlykke, K., Ramm, M., Saigal, G.C., 1989. Sandstone diagenesis and porosity modification during basin evolution. Geol. Rundsch. 78, 243–268. https:// doi.org/10.1007/BF01988363.
- Bloch, Salman, Lander, R.H., Bonnell, L., 2002. Anomalously high porosity and permeability in deeply buried sandstone reservoirs: origin and predictability. AAPG Bull. 86 (2), 301–328. https://doi.org/10.1306/61EEDABC-173E-11D7-8645000102C1865D.
- Burnie, S.W., Maini, B., Palmer, B.R., Rakhit, K., 2008. Experimental and empirical observations supporting a capillary model involving gas generation, migration, and seal leakage for the origin and occurrence of regional gasifers. In: Cumella, S.P., Shanley, K.W., Camp, W.K. (Eds.), Understanding, Exploring, and Developing Tight Gas Sands, 2005 Vail Hedberg Conference, AAPG Hedberg Series, vol. 3, pp. 29–48. https://doi.org/10.1306/1060754H23160.
- Cao, B.F., Sun, W., Li, J., 2021. Reservoir petrofacies—a tool for characterization of reservoir quality and pore structures in a tight sandstone reservoir: a study from the sixth member of Upper Triassic Yanchang Formation, Ordos Basin, China. J. Petrol. Sci. Eng. 199, 108294. https://doi.org/10.1016/ i.petrol.2020.108294.
- Comisky, J.T., Newsham, K.E., Rushing, J.A., Blasingame, T.A., 2007. A comparative study of capillary-pressure-based empirical models for estimating absolute permeability in tight gas sands, in Innovate a golden opportunity for people and technology. In: SPE Annual Technical Conference and Exhibition. Anaheim, California, p. 18. https://doi.org/10.2118/110050-MS.
- Cui, Y.F., Wang, G.W., Jones, S.J., Zhou, Z.L., Ran, Y., Lai, J., Li, R.J., Deng, L., 2017. Prediction of diagenetic facies using well logs—a case study from the upper Triassic Yanchang Formation, Ordos Basin, China. Mar. Petrol. Geol. 81, 50–65. https://doi.org/10.1016/j.marpetgeo.2017.01.001.
- Desbois, G., Urai, J.L., Kukla, P.A., Konstanty, J., Baerle, C., 2011. High-resolution 3D fabric and porosity model in a tight gas sandstone reservoir: a new approach to investigate microstructures from mm-to nm-scale combining argon beam cross-sectioning and SEM imaging. J. Petrol. Sci. Eng. 78, 243—257. https://doi.org/10.1016/j.petrol.2011.06.004.
- Dong, T., Harris, N.B., Ayranci, K., Yang, S., 2017. The impact of rock composition on geomechanical properties of a shale formation: middle and Upper Devonian Horn River Group shale, Northeast British Columbia, Canada. AAPG (Am. Assoc. Pet. Geol.) Bull. 101 (2), 177–204. https://doi.org/10.1306/07251615199.
- Dutton, S.P., Loucks, R.D., 2010. Diagenetic controls on evolution of porosity and permeability in lower Tertiary Wilcox sandstones from shallow to ultradeep (200–6700 m) burial, Gulf of Mexico Basin, U.S.A. Mar. Petrol. Geol. 27, 69–81. https://doi.org/10.1016/j.marpetgeo.2009.08.008.
- Ehrenberg, S.N., 1989. Assessing the relative importance of compaction processes and cementation to reduction of porosity in sandstones: discussion; Compaction and porosity evolution of Pliocene sandstones, Ventura Basin, California: Discussion. AAPG Bull. 73 (10), 1274—1276. https://doi.org/10.1306/44B4AA1E-170A-11D7-8645000102C1865D.
- Folk, R.L., 1980. The Petrology of Sedimentary Rocks. Hemphill Publishing Company, Austin, TX, p. 127.
- Foroshani, J.S., Mehrabi, H., Rahimpour-Bonab, H., 2023. Reservoir heterogeneity of Upper Cretaceous Sarvak Formation in the Dezful Embayment, SW Iran: Implications of flow unit distribution, electrofacies analysis and geological-based reservoir zonation. J. Afr. Earth Sci. 200, 104882. https://doi.org/10.1016/ j.jafrearsci.2023.104882.
- Freedman, R., 2006. Advances in NMR logging. J. Petrol. Technol. 58 (1), 60–66. https://doi.org/10.2118/89177-JPT.
- Gao, X.D., Wang, Y.B., Li, Y., Guo, H., Ni, X.M., Wu, X., Zhao, S.H., 2019. Characteristics of tight sandstone reservoirs and controls of reservoir quality: a case study of He 8 sandstones in the linxing area, eastern ordos basin, China. Acta Geologica Sinica-English Edition 93 (3), 637–659. https://doi.org/10.1111/1755-6724.13862.
- Guo, Q., Wang, X.Y., Yin, S., Wu, Z.H., 2021. Tectonic evolution and gas control analysis of the Upper Palaeozoic tight sandstone reservoirs in the Linxing area of the eastern Ordos Basin. Geol. J. 56 (3), 1625–1637. https://doi.org/10.1002/gj.4007.
- Hanson, A.D., Ritts, B.D., Moldowan, J.M., 2007. Organic geochemistry of oil and source rock strata of the Ordos Basin north-central China. AAPG Bull. 91 (9), 1273–1293. https://doi.org/10.1306/05040704131.
- Higgs, K.E., Arnot, M.J., Brindle, S., 2015. Advances in grain-size, mineral, and pore-scale characterization of lithic and clay-rich reservoirs. AAPG Bull. 99 (7), 1315–1348. https://doi.org/10.1306/01271513101.
- Hood, K.C., Yurewicz, D.A., 2008. Assessing the Mesaverde basin-centered gas play, Piceance Basin, Colorado. AAPG Hedberg Series (3), 87–104.
- Huang, H.X., Sun, W., Ji, W.M., Zhang, R.H., Du, K., Zhang, S.H., Ren, D.Z., Wang, Y.W., Chen, L., Zhang, X., 2018. Effects of pore-throat structure on gas permeability in the tight sandstone reservoirs of the Upper Triassic Yanchang formation in the Western Ordos Basin, China. J. Petrol. Sci. Eng. 162, 602–616. https://doi.org/ 10.1016/j.petrol.2017.10.076.
- Imamverdiyev, Y., Sukhostat, L., 2019. Lithological facies classification using deep convolutional neural network. Journal of Petroleim Science and Engineering

- 174, 216-228. https://doi.org/10.1016/j.petrol.2018.11.023.
- Jacobsen, S., May, D., Grant, J. Little J., 2006. Producibility Prediction in Gas Sands Through Effective Integration of NMR, Resistivity, and Porosity Log Data. In: Transactions of the SPWLA 47th Annual Logging Symposium, June 4–7.
- Jarvie, D.M., Hill, R.J., Ruble, T.E., Pollastro, R.M., 2007. Unconventional shale-gas systems: The Mississippian Barnett Shale of north-central Texas as one model for thermogenic shale-gas assessment. AAPG Bull. 91 (4), 475–499. https:// doi.org/10.1306/12190606068.
- Kadkhodaie-Ilkhchi, R., Rezaee, R., Moussavi-Harami, R., Kadkhodaie-Ilkhchi, A., 2013. Analysis of the reservoir electrofacies in the framework of hydraulic flow units in the Whicher Range field, Perth Basin, western Australia. J. Petrol. Sci. Eng. 111, 106–120. https://doi.org/10.1016/j.petrol.2013.10.014.
- Khlaifat, A., Qutob, H., Barakat, N., 2011. Tight gas sands development is critical to future world energy resources. In: SPE Middle East Unconventional Resources Conference and Exhibition. https://doi.org/10.2118/142049-MS. SPE-142049). SPE
- Kim, J., 2022. Lithofacies classification integrating conventional approaches and machine learning technique. J. Nat. Gas Sci. Eng. 100, 104500. https://doi.org/ 10.1016/j.ingse.2022.104500
- Lai, J., Wang, G.W., Fan, Z.Y., Chen, J., Wang, S.C., Zhou, Z.L., Fan, X.Q., 2016. Insight into the pore structure of tight sandstones using NMR and HPMI measurements. Energy Fuel. 30 (12), 10200–10214. https://doi.org/10.1021/acs.energyfuels.6b01982.
- Lai, J., Wang, G.W., Wang, Z.Y., Chen, J., Pang, X.J., Wang, S.C., Zhou, Z.L., He, Z.B., Qin, Z.Q., Fan, X.Q., 2018a. A review on pore structure characterization in tight sandstones. Earth Sci. Rev. 177, 436–457. https://doi.org/10.1016/ j.earscirev.2017.12.003.
- Lai, J., Wang, G.W., Wang, S.C., Cao, J.T., Li, M., Pang, X.J., Zhou, Z.L., Fan, X.Q., Dai, Q.Q., Liu, Y., He, Z.B., Qin, Z.Q., 2018b. Review of diagenetic facies in tight sandstones: Diagenesis, diagenetic minerals, and prediction via well logs. Earth Sci. Rev. 185, 234–258. https://doi.org/10.1016/j.earscirev.2018.06.009.
- Lai, J., Fan, X.C., Pang, X.J., Zhang, X.S., Xiao, C.W., Zhao, X.J., Han, C., Wang, G.W., Qin, Z., 2019. Correlating diagenetic facies with well logs (conventional and image) in sandstones: The Eocene—Oligocene Suweiyi Formation in Dina 2 Gasfield, Kuqa depression of China. J. Petrol. Sci. Eng. 174, 617–636. https://doi.org/10.1016/j.petrol.2018.11.061.
- Lai, J., Fan, X.C., Liu, B.C., Pang, X.J., Zhu, S.F., Xie, W.B., Wang, G.W., 2020. Qualitative and quantitative prediction of diagenetic facies via well logs. Mar. Petrol. Geol. 120, 104486. https://doi.org/10.1016/j.marpetgeo.2020.104486.
- Law, B.E., Curtis, J.B., 2002. Introduction to unconventional petroleum systems. AAPG Bull. 86 (11), 1851–1852. https://doi.org/10.1306/61EEDDA0-173E-11D7-8645000102C1865D.
- Li, J.Q., Wang, S.Y., Lu, S.F., Zhang, P.F., Cai, J.C., Zhao, J.H., Li, W.B., 2019. Micro-distribution and mobility of water in gas shale: a theoretical and experimental study. Mar. Petrol. Geol. 102, 496–507. https://doi.org/10.1016/j.marpetgeo.2019.01.012.
- Li, J., Zhang, X., Tian, J.C., Liang, Q.S., Cao, T.S., 2021. Effects of deposition and diagenesis on sandstone reservoir quality: A case study of Permian sandstones formed in a braided river sedimentary system, northern Ordos Basin, Northern China. J. Asian Earth Sci. 213, 104745. https://doi.org/10.1016/ j.jseaes.2021.104745.
- Liu, H.P., Zhao, Y.C., Luo, Y., Chen, Z.Y., He, S., 2015. Diagenetic facies controls on pore structure and rock electrical parameters in tight gas sandstone. J. Geophys. Eng. 12 (4), 587–600. https://doi.org/10.1088/1742-2132/12/4/587.
- Liu, J.L., Liu, K.Y., Huang, X., 2016. Effect of sedimentary heterogeneities on hydrocarbon accumulations in the Permian Shanxi Formation, Ordos Basin, China: Insight from an integrated stratigraphic forward and petroleum system modelling. Mar. Petrol. Geol. 76, 412–431. https://doi.org/10.1016/j.marpetgeo.2016.05.028.
- Liu, Q.Q., Chen, G.H., Chen, X.Z., Zhu, Y.H., Yang, X.F., 2018. Characteristic of provenance and its impact on reservoir quality of Upper Shihezi Formation, L block, Ordos Basin. Nat. Gas Geosci. 29, 1094–1101. https://doi:10.11764/j.issn. 16721926.2018.05.007 (in Chinese).
- Liu, X.J., Ma, Z.J., Hang, D., Wang, H.Y., Ma, L.T., Ge, D.S., 2018. Natural Gas Geoscience Research on the main factors of high quality tight sandstone reservoir in Linxing block, Ordos Basin. Nat. Gas Geosci. 29, 481–490. https://doi:10.11764/j.issn.16721926.2018.02.002 (in Chinese).
- Loyd, S.J., Corsetti, F.A., Eiler, J.M., Tripati, A.K., 2012. Determining the diagenetic conditions of concretion formation: assessing temperatures and pore waters using clumped isotopes. J. Sediment. Res. 82, 1006–1016. https://doi.org/ 10.2110/isr.2012.85.
- Ma, Y.Z., 2016. Unconventional resources from exploration to production. In: Unconventional Oil and Gas Resources Handbook. Gulf Professional Publishing, pp. 3–52. https://doi.org/10.1016/B978-0-12-802238-2.00001-8.
- Ma, Y.Z., Gomez, E., 2015. Uses and abuses in applying neural networks for predictions in hydrocarbon resource evaluation. J. Petrol. Sci. Eng. 133, 66-75. https://doi.org/10.1016/j.petrol.2015.05.006.
- Ma, Y.Z., Moore, W.R., Gomez, E., Clark, W.J., Zhang, Y., 2016. Tight gas sandstone reservoirs, Part 1: Overview and lithofacies. Unconventional Oil and Gas Resources Handbook 405–427. https://doi.org/10.1016/B978-0-12-802238-2.00014-6.
- Mckinley, J.M., Atkinson, P.M., Lloyd, C.D., Ruffell, A.H., Worden, R.H., 2011. How porosity and permeability vary spatially with grain size, sorting, cement volume, and mineral dissolution in fluvial Triassic sandstones: the value of geostatistics and local regression. J. Sediment. Res. 81, 844–858. https://doi.org/

10.2110/isr.2011.71.

- Meckel, L., Thomasson, M., 2008. Pervasive tight-gas sandstone reservoirs: An overview. AAPG Hedberg Series (3), 13–27. https://doi.org/10.1306/13131047H33321.
- Mehrabi, H., Bagherpour, B., 2022. Scale, origin, and predictability of reservoir heterogeneities in shallow-marine carbonate sequences: A case from Cretaceous of Zagros, Iran. J. Petrol. Sci. Eng. 214, 110571. https://doi.org/10.1016/ i.petrol.2022.110571.
- Mehrabi, H., Esrafili-Dizaji, B., Hajikazemi, E., Noori, B., Mohammad-Rezaei, H., 2019a. Reservoir characterization of the Burgan Formation in northwestern Persian Gulf. J. Petrol. Sci. Eng. 174, 328–350. https://doi.org/10.1016/ i.petrol.2018.11.030.
- Mehrabi, H., Ranjbar-Karami, R., Roshani-Nejad, M., 2019b. Reservoir rock typing and zonation in sequence stratigraphic framework of the Cretaceous Dariyan Formation, Persian Gulf. Carbonates Evaporites 34, 1833–1853. https://doi.org/ 10.1007/s13146-019-00530-2.
- Mi, L.J., Zhu, G.H., 2021. Geological characteristics and exploration breakthrough in Linxing-Shenfu Tight Gas Field, northeastern Ordos Basin. China Petroleum Exploration 26. 53. https://10.3969/i.issn.1672-7703.2021.03.005 (in Chinese).
- Midtbø, R.E.A., Rykkje, J.M., Ramm, M., 2000. Deep burial diagenesis and reservoir quality along the eastern flank of the Viking Graben. Evidence for illitization and quartz cementation after hydrocarbon emplacement. Clay Miner. 35 (1), 227–237. https://doi.org/10.1180/000985500546602.
- Misra, S., Li, H., He, J., 2019. Machine Learning for Subsurface Characterization. Gulf Professional Publishing.
- Morad, S., Al-Ramadan, K., Ketzer, J.M., De Ros, L.F., 2010. The impact of diagenesis on the heterogeneity of sandstone reservoirs: A review of the role of depositional facies and sequencestratigraphy. AAPG Bull. 94 (8), 1267–1309. https://doi.org/10.1306/04211009178.
- Nabawy, B.S., Géraud, Y., 2015. Impacts of pore- and petro-fabrics, mineral composition and diagenetic history on the bulk thermal conductivity of sand-stones. J. Afr. Earth Sci. 115, 21–24. https://doi.org/10.1016/j.jafrearsci.2015.11.025.
- Nabawy, B.S., Géraud, Y., Rochette, P., Bur, N., 2009. Pore-throat characterization in highly porous and permeable sandstones. AAPG Bull. 93, 719–739. https://doi.org/10.1306/03160908131.
- Nguyen, B.T.T., Jones, S.J., Goulty, N.R., Middleton, A.J., Grant, N., Ferguson, A., Bowen, L., 2013. The role of fluid pressure and diagenetic cements for porosity preservationin Triassic fluvial reservoirs of the Central Graben, North Sea. AAPG Bull. 97 (8), 1273–1302. https://doi.org/10.1306/01151311163.
- Peters, K.E., Xia, X., Pomerantz, A.E., Mullins, O.C., 2016. Geochemistry applied to evaluation of unconventional resources. In: Unconventional Oil and Gas Resources Handbook. Gulf Professional Publishing, pp. 71–126. https://doi.org/ 10.1016/B978-0-12-802238-2.00003-1.
- Pittman, E.D., 1992. Relationship of porosity and permeability to various parameters derived from mercury injection capillary pressure curves for sandstone. AAPG Bull. 76 (2), 191–198. https://doi.org/10.1306/BDFF87A4-1718-11D7-8645000102C1865D.
- Pratama, E., Suhaili Ismail, M., Ridha, S., 2017. An integrated workflow to characterize and evaluate low resistivity pay and its phenomenon in a sandstone reservoir. J. Geophys. Eng. 14 (3), 513–519. https://doi.org/10.1088/1742-2140/aa5eth
- Qi, Y., Ju, Y.W., Meng, S.Z., Yu, K., Li, W.Y., Jia, T.R., Wu, J.G., Chen, W.G., Luo, L., 2020. Geological controls on high production of tight sandstone gas in Linxing Block, Eastern Ordos Basin, China. Acta Geologica Sinica-English Edition 94 (2), 430–443. https://doi.org/10.1111/1755-6724.14334.
- Qiao, J.C., Zeng, J.H., Jiang, S., Wang, Y.N., 2020. Impacts of sedimentology and diagenesis on pore structure and reservoir quality in tight oil sandstone reservoirs: implications for macroscopic and microscopic heterogeneities. Mar. Petrol. Geol. 111, 279–300. https://doi.org/10.1016/j.marpetgeo.2019.08.008.
- Rahimpour-Bonab, H., Mehrabi, H., Navidtalab, A., Izadi-Mazidi, E., 2012. Flow unit distribution and reservoir modelling in cretaceous carbonates of the Sarvak Formation, Abteymour Oilfield, Dezful Embayment, SW Iran. J. Petrol. Geol. 35 (3), 213–236. https://doi.org/10.1111/j.1747-5457.2012.00527.x.
- Rezaee, M.R., Lemon, N.M., 1996. Influence of depositional environment on diagenesis and reservoir quality: Tirrawarra Sandstone reservoir, Southern Cooper Basin, Australia. J. Petrol. Geol. 19 (4), 369–391. https://doi.org/10.1111/ j.1747-5457.1996.tb00445.x.
- Ribacchi, R., 2000. Mechanical tests on pervasively jointed rock material: insight into rock mass behaviour. Rock Mech. Rock Eng. 33, 243–266. https://doi.org/ 10.1007/s006030070002.
- Rider, M., Kennedy, M., 2011. The Geological Interpretation of Well Logs: Rider-French Consulting Limited.
- Rossi, C., Marfil, R., Ramseyer, K., Permanyer, A., 2001. Facies-related diagenesis and ultiphase siderite cementation and dissolution in the reservoir sandstones of the hatatba Formation, Egypt's Western Desert. J. Sediment. Res. 71 (3), 459–472. https://doi.org/10.1306/2DC40955-0E47-11D7-8643000102C1865D.
- Rushing, J.A., Newsham, K.E., Blasingame, T.A., 2008. Rock typing—Keys to understanding productivity in tight gas sands. In: SPE Unconventional Resources Conference/Gas Technology Symposium. https://doi.org/10.2118/114164-MS. SPE-114164). SPE.
- Sadhukhan, S., Dutta, T., Tarafdar, S., 2007. Simulation of diagenesis and permeability variation in two-dimensional rock structure. Geophys. J. Int. 169 (3), 1366–1375. https://doi.org/10.1111/j.1365-246X.2007.03426.x.
- Samakinde, C., Opuwari, M., van Bever Donker, J.M., 2016. The effects of clay

- diagenesis on petrophysical properties of the lower Cretaceous sandstone reservoirs, Orange Basin, South Africa. S. Afr. J. Geol. 119 (1), 187–202. https://doi.org/10.2113/gssajg.119.1.187.
- Schön, J.H., 2015. Physical Properties of Rocks: Fundamentals and Principles of Petrophysics. Elsevier.
- Shanley, K.W., Cluff, R.M., Robinson, J.W., 2004. Factors controlling prolific gas production from low-permeability sandstone reservoirs: Implications for resource assessment, prospect development, and risk analysis. AAPG Bull. 88, 1083—1121. https://doi.org/10.1306/03250403051.
- Shu, Y., Lin, Y.X., Liu, Y., Yu, Z.Y., 2019. Control of magmatism on gas accumulation in Linxing area, Ordos Basin, NW China: Evidence from fluid inclusions. J. Petrol. Sci. Eng. 180, 1077–1087. https://doi.org/10.1016/j.petrol.2019.06.034.
- Shu, Y., Sang, S.X., Lin, Y.X., Zhou, X.Z., Wang, H., Wang, Z.L., 2021. The influence of magmatic-hydrothermal activities on porosity and permeability of sandstone reservoirs in the Linxing area, Ordos Basin, Northern China. J. Asian Earth Sci. 213, 104741. https://doi.org/10.1016/j.jseaes.2021.104741.
- Siebert, R.M., Moncure, G.K., Lahann, R.W., 1984. A theory of framework grain dissolution in sandstones: Part 2. Aspects of Porosity Modification. https://doi.org/10.1306/M37435C10
- Solanet, F., Khatchikian, A., Breda, E., 1998. NMR as Standard Porosity Tool in the San Jorge Basin: Log Responses and Applications. SPE Reservoir Eval. Eng. 1, 504–508. https://doi.org/10.2118/52939-PA. SPE-52939-PA.
- Sun, J.P., Dong, Y.P., 2019. Triassic tectonic interactions between the Alxa Massif and Ordos Basin: Evidence from integrated provenance analyses on sandstones, North China. J. Asian Earth Sci. 169, 162–181. https://doi.org/10.1016/i.jseaes.2018.08.002.
- Swanson, B.F., 1981. A simple correlation between permeabilities and mercury capillary pressures. J. Petrol. Technol. 33 (12), 2498–2504. https://doi.org/ 10.2118/8234-PA.
- Virolle, M., Brigaud, B., Beaufort, D., Patrier, P., Abdelrahman, E., Thomas, H., Portier, H., Samson, Y., Bourillot, R., Féniès, H., 2022. Authigenic berthierine and incipient chloritization in shallowly buried sandstone reservoirs: Key role of the source-to-sink context. GSA Bulletin 134 (3–4), 739–761. https://doi.org/10.1130/B35865.1.
- Wang, Z.Y., Liu, Y.C., Lu, S.F., Zhou, N.W., Lin, L.M., Liu, Y., 2023a. Characterizations of Middle–Lower Triassic Reservoir Quality and Gas Accumulations in the Northeastern Margin of the Ordos Basin, China. Energy Fuel. 37 (11), 7823–7833. https://doi.org/10.1021/acs.energyfuels.3c00820.
- Wang, Z.Y., Liu, Y.C., Lu, S.F., Lin, L.M., Zhou, N.W., Liu, Y., 2023b. Differential development characteristics of secondary pores and effects on pore structure and movable fluid distribution in tight gas sandstones in the lower Permian, northeastern Ordos Basin, China. Geoenergy Science and Engineering 224, 211580. https://doi.org/10.1016/j.geoen.2023.211580.
- Wang, Z.Y., Zhou, N.W., Lu, S.F., Liu, Y., Lin, L.M., Liu, Y., Song, B., 2023c. Generation, accumulation, and distribution of Upper Paleozoic tight sandstone gas in the northeastern margin of the Ordos Basin. Mar. Petrol. Geol. 156, 106463. https://doi.org/10.1016/j.marpetgeo.2023.106463.
- Wang, Z.Y., Lu, S.F., Zhou, N.W., Liu, Y., Lin, L.M., Shang, Y.X., Xiao, G.S., Wang, J., 2023d. Diagenesis as a control on the tight sandstone reservoir quality of the upper Carboniferous strata in the northeastern Ordos basin, China. Mar. Petrol. Geol. 158, 106565. https://doi.org/10.1016/j.marpetgeo.2023.106565.
- Wei, Z.L., Hu, H., Zhou, H.W., Lau, A., 2019. Characterizing rock facies using machine learning algorithm based on a convolutional neural network and data padding strategy. Pure Appl. Geophys. 176 (8), 3593—3605. https://doi.org/10.1007/ s00024-019-02152-0.
- Worden, R.H., Burley, S.D., 2003. Sandstone diagenesis: the evolution of sand to stone. Sandstone diagenesis: Recent and ancient. International Association of Sedimentologists 4, 3–44.
- Xiao, X.M., Zhao, B.Q., Thu, Z.L., Song, Z.G., Wilkins, R.W.T., 2005. Upper Paleozoic petroleum system, Ordos Basin, China. Mar. Petrol. Geol. 22, 945–963. https://doi.org/10.1016/j.marpetgeo.2005.04.001.
- Xiao, D.S., Lu, Z.Y., Jiang, S., Lu, S.F., 2016. Comparison and integration of experimental methods to characterize the full-range pore features of tight gas sandstone—A case study in Songliao Basin of China. J. Nat. Gas Sci. Eng. 34, 1412–1421. https://doi.org/10.1021/acs.energyfuels.7b01487.
- Xiao, D.S., Lu, S.F., Yang, J.X., Zhang, L.C., Li, B., 2017. Classifying multiscale pores and investigating their relationship with porosity and permeability in tight sandstone gas reservoirs. Energy Fuel. 31 (9), 9188–9200. https://doi.org/10.1021/acs.energyfuels.7b01487.
- Yang, Y.T., Li, W., Ma, L., 2005. Tectonic and stratigraphic controls of hydrocarbon systems in the Ordos basin: A multicycle cratonic basin in central China. AAPG Bull. 89 (2), 255–269. https://doi.org/10.1306/10070404027.
- Zhang, P.F., Lu, S.F., Li, J.Q., Chen, C., Xue, H.T., Zhang, J., 2018. Petrophysical characterization of oil-bearing shales by low-field nuclear magnetic resonance (NMR). Mar. Petrol. Geol. 89, 775–785. https://doi.org/10.1016/j.marpetgeo.2017.11.015.
- Zou, C.N., Tao, S.Z., Zhou, H., Zhang, X.X., He, D.B., Zhou, C.M., Wang, L., Wang, X.S., Li, F.H., Zhu, R.K., Luo, P., Yuan, X.J., Xu, C.C., Yang, H., 2008. Genesis, classification, and evaluation method of diagenetic facies. Petrol. Explor. Dev. 35, 526–540. https://doi.org/10.1016/S1876-3804(09)60086-0.
- Zou, C.N., Yang, Z., Tao, S.Z., Yuan, X.J., Zhu, R.K., Hou, L.H., Wu, S.T., Sun, L., Zhang, G.S., Bai, B., Wang, L., Gao, X.H., Pang, Z.L., 2013. Continuous hydrocarbon accumulation over a large area as a distinguishing characteristic of unconventional petroleum: The Ordos Basin, North-Central China. Earth Sci. Rev. 126, 358–369. https://doi.org/10.1016/j.earscirev.2013.08.006.